Materials Horizons

ROYAL SOCIETY OF CHEMISTRY

REVIEW

View Article Online
View Journal

Check for updates

Cite this: DOI: 10.1039/d2mh00279e

Concepts and principles of self-n-doping in perylene diimide chromophores for applications in biochemistry, energy harvesting, energy storage, and catalysis

Daniel Powell* and Luisa Whittaker-Brooks *

Received 4th March 2022,
Accepted 31st May 2022

DOI: 10.1039/d2mh00279e

rsc.li/materials-horizons

Self-doping is an essential method of increasing carrier concentrations in organic electronics that eliminates the need to tailor host—dopant miscibility, a necessary step when employing molecular dopants. Self-n-doping can be accomplished using amines or ammonium counterions as an electron source, which are being incorporated into an ever-increasingly diverse range of organic materials spanning many applications. Self-n-doped materials have demonstrated exemplary and, in many cases, benchmark performances in a variety of applications. However, an in-depth review of the method is lacking. Perylene diimide (PDI) chromophores are an important mainstay in the semiconductor literature with well-known structure-function characteristics and are also one of the most widely utilized scaffolds for self-n-doping. In this review, we describe the unique properties of self-n-doped PDIs, delineate structure-function relationships, and discuss self-n-doped PDI performance in a range of applications. In particular, the impact of amine/ammonium incorporation into the PDI scaffold on doping efficiency is reviewed with regard to attachment mode, tether distance, counterion selection, and steric encumbrance. Self-n-doped PDIs are a unique set of PDI structural derivatives whose properties are amenable to a broad range of applications such as biochemistry, solar energy conversion, thermoelectric modules, batteries, and photocatalysis. Finally, we discuss challenges and the future outlook of self-n-doping principles.

Department of Chemistry, University of Utah, Salt Lake City, Utah, 84112, USA.
E-mail: danny.powell@chem.utah.edu, luisa.whittaker@utah.edu

1. Introduction

Doping is essential in achieving any functional organic semiconductor with a high carrier concentration regardless of its

Daniel Powell

Daniel Powell received his PhD from the Department of Chemistry at The University of Utah. His primary research interests focus on developing and understanding electronic doping strategies in semiconducting materials. His research also involves developing novel characterization approaches of materials with an emphasis on automated robotics and machine learning approaches.

Luisa Whittaker-Brooks

Luisa Whittaker-Brooks is an Associate Professor of Chemistry at the University of Utah. Her research centers on the design of well-defined hybrid materials with controlled morphology and interfaces that serve as conduits for deterministic and coherent energy and charge transfer for applications in energy conversion, storage, and electronics. She received her BS in Chemistry from The University of Panama. Under a Fulbright Fellowship, she received her PhD in Chemistry from the University at Buffalo. She was a postdoctoral researcher at Princeton University under a L'Oréal for Women in Science Fellowship.

p/n-type categorization. A common method of n-type doping in organic semiconductors is to treat them with inorganic species that have relatively small ionization potentials (*e.g.*, hydrazine vapor, iodine vapor, sodium metal, *etc.*) or, more commonly, to combine them with other organic compounds with relatively low electron affinity.[1–4] This is typically accomplished by combining the dopant with the host in the solution phase and casting the mixture into thin films. In many instances, the dopants tend to aggregate together and phase segregate from the host, ultimately altering the morphology of the resulting solid-state matrix. Thus, when the solubility properties of the host and the dopant are even modestly dissimilar from one another, it presents a significant challenge for the fabrication of functional organic materials.[5] Obtaining a homogenous mixture of dopant and organic semiconductor in solution is non-trivial. The process is made even more challenging when accounting for the role of solvent evaporation during film casting. Improving host/dopant miscibility is a prominent topic in the field. Researchers must select from a variety of available methods to optimize their procedure, and the process is generally approached through trial and error.[6–8] Self-doping has emerged as a promising method of tuning carrier concentrations in small molecule organic semiconductors because it axiomatically mitigates dopant phase segregation and aggregation.

Any single molecule or polymer subunit that contains both an electron donor and electron acceptor can generally be regarded as a self-doping system, and its p-type or n-type categorization will depend on the ionization potentials of the donor and acceptor components. While self-p-doping has long been utilized in polymers,[9–11] self-n-doping remains comparatively underutilized. It has long been known that small molecules can be functionalized with various alkylamino substituents to create intramolecular donor-acceptor scaffolds.[12–17] However, only in more recent years has the technique risen to a level of prominence that has warranted an in-depth review. Primary, secondary, and tertiary amines, as well as quaternary ammonium salts, have been incorporated into a wide variety of small molecule and polymer scaffolds for their ability to act as covalently bound dopants. They have been used in a range of materials research fields, such as in low-dimensional perovskite-related hybrids, electron transporting materials in solar cells, thermoelectric composites, work function modifiers, and more.[18–32] While the chemical structures of the self-n-doped semiconductors seen across the literature are diverse, the most common derivatives are fullerenes, perylene diimides, naphthalene diimides, and fluorenes, as shown in Fig. 1. Each scaffold shown here exhibits a unique set of intrinsic physicochemical properties. The manner in which these properties are altered by the addition of amine/ammonium functional groups is non-trivial, and indeed may not be universal among the various host materials. For example, the limitations of anion reduction in self-n-doped fullerenes are disputed,[33–35] but well established in self-n-doped fluorene derivatives.[36] In the interest of providing a thorough and in-depth review, we have limited our discussion to what is arguably the most common scaffold: perylene diimides (PDIs).

N,*N*′-Disubstituted perylene-3,4,9,10-tetracarboxylic acid imides (PDIs) are chromophores belonging to the rylene dye family that were initially used as red vat dyes following their

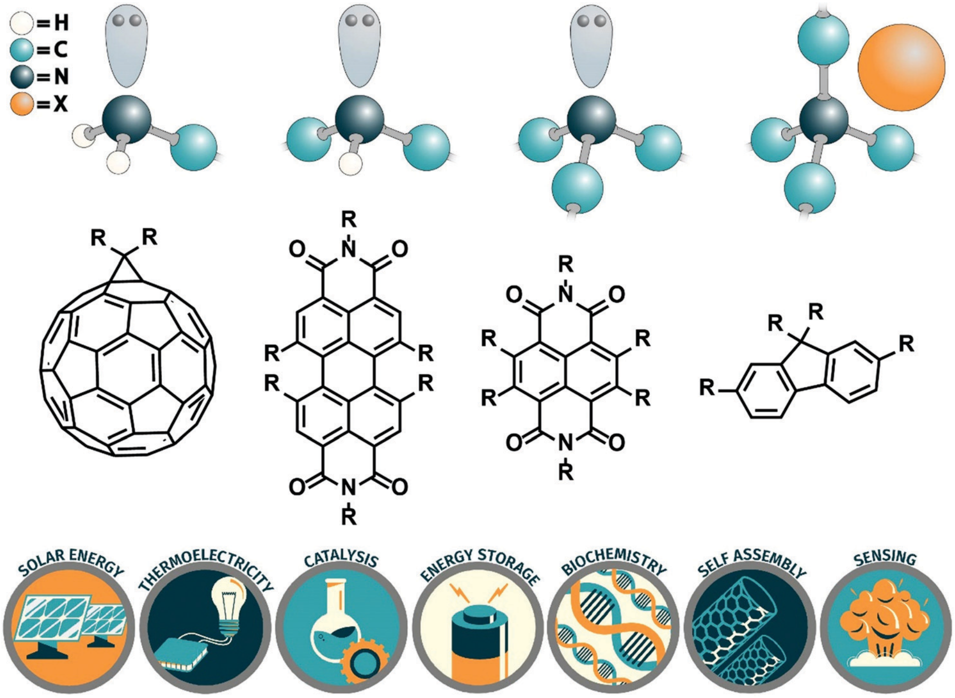

Fig. 1 Primary, secondary, and tertiary amines and quaternary ammonium salt dopant structures are shown at the top. The generalized chemical structures of acceptor motifs commonly observed in the literature are shown in the center; from left to right, fullerene, perylene diimide, naphthalene diimide, and fluorene. Animated depictions of the many applications of these materials are shown at the bottom.

development in 1913, and by the late 1950s became fully commercialized as pigments commonly used in automobile paints and other dye applications.[37] Today, these dyes are used in ways never imagined by their inventors and are one of the most heavily investigated small molecules in the organic semiconductor community.[38–40] These chromophores have found application in a surprising breadth of fields, including fluorescence spectroscopy, sensing, supramolecular assemblies, and more.[41–43] Ease of synthesis, synthetic modularity, high thermal stability, high oscillator strengths, and large fluorescence quantum yields are a few of the reasons these dyes have garnered so much attention.[44] The rise in interest in PDIs has naturally coincided with the field growing progressively more specialized. A given application requires very specific material properties. Consequently, much of the information available on self-n-doped PDIs is fragmented into application-specific citation clusters. This review presents self-n-doped materials as a class of structural derivate whose unique and exciting physicochemical properties merit their distinct categorization. We anticipate that the information reviewed here will be useful to researchers spanning a breadth of fields as we discuss this emerging and often misunderstood material class.

Self-n-doped PDIs are characterized by a perylene diimide scaffold functionalized with one or more amine or ammonium substituents at one or more R-group locations, which we refer to as N-PDIs (amino-functionalized PDIs), as shown in Fig. 1. Here, one or more R groups will contain an amine or ammonium salt within any carbon chain or cycle, while the remaining R groups may be composed of hydrogen, any carbon chain, any carbon cycle, or any heteroatom. X corresponds to any monovalent or multivalent anionic counterion. Incorporating amines or ammonium salts into the PDI scaffold strongly affects the material's excited state dynamics and electronic properties. Consequently, PDIs have exhibited great promise in a wide range of applications both in solution and in the solid-state, such as nano and sub-nanomolar chemical probes for biological and chemical sensing, protein inhibition, photocatalysis, controllable self-assembly, thin-film polarizers, photovoltaics, thermoelectrics, and batteries.[45–55] A selection of these applications is discussed in greater detail in Section 3. We have consolidated the information available on N-PDIs to provide insights into the functionality of self-n-doped materials and delineate how these properties make them promising candidates in such a wide range of applications.

2. General properties of PDIs

2.1 Monomers

The photophysical properties of PDIs are rich and have been the subject of critical investigation.[56,57] The acceptor–donor–acceptor (A–D–A) PDI scaffold sandwiches the electron abundant perylene between inductively withdrawing dicarboxylic acid imides, which induces a bathochromic shift in the absorption spectrum by ~100 nm relative to perylene. The characteristic absorption peaks of PDI, shown in Fig. 2A, originate from the perylene core.[58] These absorption peaks correspond to ground state $S_0 \rightarrow S_1$ Franck–Condon vibronic transitions 0–0, 0–1, 0–2, and 0–3 that are typically found in the range of ~420

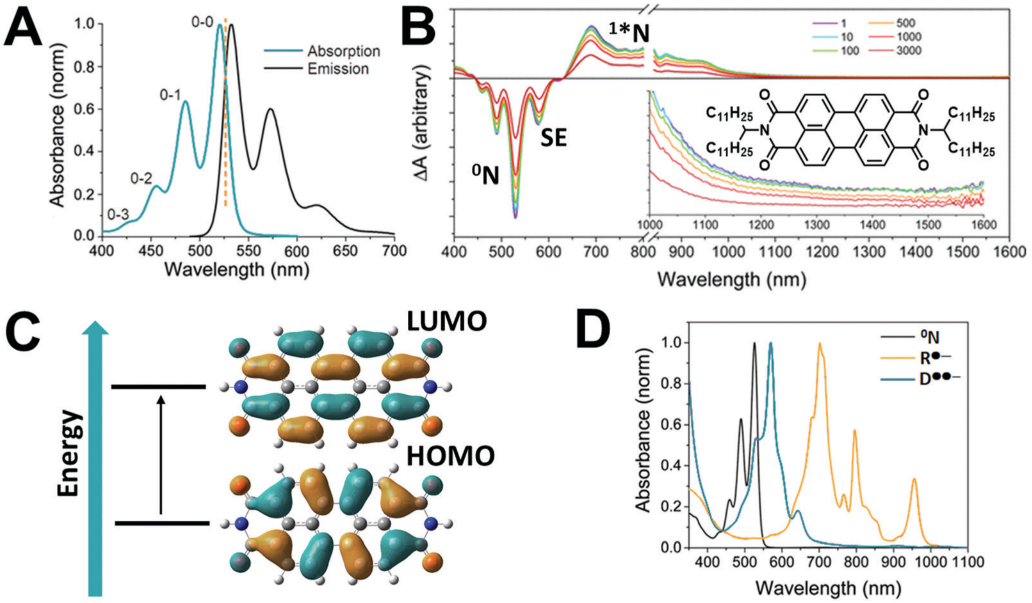

Fig. 2 (A) Prototypical absorption/emission spectra of PDI monomers in solution. Adapted with permission from ref. 58. Copyright 2015 American Chemical Society. (B) Visible/NIR femtosecond transient absorption spectra of a PDI (structure in inset) excited at 525 nm and time delays reported in ps. Reprinted with permission from ref. 61. Copyright 2014 American Chemical Society. (C) Gaussian simulated molecular orbitals of PDI's HOMO and LUMO computed at the DFT level using the B3LYP functional and a 6-311G** basis set. (D) Characteristic absorption spectra of PDI monomer (black), PDI radical anion (orange), and PDI diradical dianion (blue). Adapted from ref. 68. Copyright 2017 The Royal Society of Chemistry.

to ~530 nm, and the emission spectrum is a mirror-image of the absorption spectrum.[59,60] Transient absorption characteristics of PDIs are shown in Fig. 2B, which typically involve an $S_0 \rightarrow S_1$ ground state (${}^{\mathbf{0}}\mathbf{N}$) bleach from ~420–530 nm that is often accompanied by stimulated emission at ~590 nm. Concomitant with the ground state bleach is the growth of a photoinduced absorption transient at ~690 nm tailing into the NIR that is attributed to the excited singlet state (${}^{\mathbf{1}*}\mathbf{N}$) absorption $S_1 \rightarrow S_n$ ($n > 1$).[61] In general, ${}^{\mathbf{1}*}\mathbf{N}$ quickly relaxes (a few ns) back to the ground state (${}^{\mathbf{0}}\mathbf{N}$). Intersystem crossing is typically not observed in PDI monomers as the triplet state energy level is relatively low-lying from S_1, and their rigidity makes radiationless internal conversion very slow. PDI monomers thus typically exhibit fluorescence quantum yields near unity and have excellent photostability.[62] However, there are cases in which the triplet intermediate may be accessed. For example, in thionated PDI systems or those within a coordination complex.[63–65]

The highest occupied molecular orbital (HOMO) and the lowest unoccupied molecular orbital (LUMO) are localized to the perylene core, as shown in Fig. 2C. Functionalization of the perylene core is the primary method of altering the HOMO/LUMO energy levels of the PDI chromophore. Hypsochromic or bathochromic shifting and dramatic shifts in redox potential can be observed depending on the electron-withdrawing or donating ability of the added group. As a result, the colors of fully solvated PDIs in solution are strongly dependent on the choice of the functional group. The energy of the $S_0 \rightarrow S_1$ transition remains largely unchanged when functionalizing PDIs at the imide positions due to the transverse node in the core HOMO and LUMO orbitals of the perylene scaffold. As such, the imide groups are not electrically connected to the core.[44] More recent work has shown that thionation of the dicarboxylic acid imides can also dramatically decrease the LUMO energy, resulting in a red shift of the $S_0 \rightarrow S_1$ transition.[64,66,67]

PDI monomers are also capable of bearing stable radical anions ($\mathbf{R}^{\bullet-}$) and dianions ($\mathbf{D}^{\bullet\bullet-}$). Absorption spectra of a PDI chemically reduced with tetrakis(dimethylamino)ethylene (TDAE) to form $\mathbf{R}^{\bullet-}$ and reduced with cobaltacene ($CoCp_2$) to form $\mathbf{D}^{\bullet\bullet-}$ are shown in Fig. 2D with ${}^{0}\mathbf{N}$ shown for ref. 68 $\mathbf{R}^{\bullet-}$ has six characteristic absorption peaks from ~680 to ~955 nm, with the ~955 nm feature corresponding to the $D_0 \rightarrow D_1$ transition accompanied by a complex vibronic structure. The singlet transitions of $\mathbf{D}^{\bullet\bullet-}$ are blue-shifted from the doublet transitions of $\mathbf{R}^{\bullet-}$ and have five major peaks from ~530–720 nm. Gosztola *et al.* have shown the lifetimes of ${}^{2*}\mathbf{R}^{\bullet-}$ excited states are generally much shorter than ${}^{\mathbf{1}*}\mathbf{N}$, which likely contributes to the radical anion's exceptional photostability. The absorption spectra of $\mathbf{R}^{\bullet-}$ and ${}^{\mathbf{1}*}\mathbf{N}$ are very similar because both exist at similar energies and involve the LUMO of ${}^{0}\mathbf{N}$. In the case of $\mathbf{R}^{\bullet-}$, an electrochemical reduction places an electron in the LUMO of ${}^{0}\mathbf{N}$, which can then be further excited to $D_0 \rightarrow D_n$. In the case of ${}^{\mathbf{1}*}\mathbf{N}$, an electron from the HOMO of ${}^{0}\mathbf{N}$ is excited into the LUMO and can then be further excited to $S_1 \rightarrow S_n$. The LUMO energy is not strongly affected when it is populated with one or two electrons.[69]

2.2 Aggregates

The absorption, photoluminescence, and excited-state dynamics of PDIs are dramatically altered by their assembly into dimer aggregates and beyond.[70] PDI aggregates are held together by weak van der Waals forces. As chromophores aggregate, the HOMO and LUMO orbital wavefunctions overlap. The electron-hole pairs can then delocalize over all of the chromophores in the dimer, which splits the energy of the $S_0 \rightarrow S_1$ transition into two Frenkel excitonic states. The ground and excited state energies of aggregates decrease compared to monomers because the electrically polarized $S_0 \rightarrow S_1$ exciton induces dipole-dipole interactions between adjacent chromophores. Changes in the absorption spectrum of aggregated chromophores are described by Kasha's exciton coupling theory which relates the relative geometries of adjacent chromophores to their transition dipole moments. In its most basic description, molecules with side-by-side transition dipoles form H-aggregates, and their absorption spectra are shifted hypsochromically. In contrast, head-to-tail transition dipoles form J-aggregates, and their absorption spectra are shifted bathochromically. Additionally, the fluorescence quantum yield decreases in both aggregate systems, while the radiative decay rate is decreased in H-aggregates and enhanced in J-aggregates.[71,72] In reality, the situation is more complex as the Kasha model does not take into account vibronic fine structure and is limited to Coulomb coupling between chromophores. Furthermore, Kazmaier *et al.* demonstrated that the electron and hole transfer integrals, which dictate the valence and conduction bandwidths, are not entirely described by the overlap between wave functions on adjacent chromophores, but that they also depend on a quantum interference effect that is highly sensitive to slight transverse chromophore displacements. A schematic energy level diagram depicting the charge transfer between neighboring chromophores is shown in Fig. 3A, where E_{CT} is the resonance energy of the charge transfer exciton, t_e and t_h are the electron and hole transfer integrals, and J_{CT} is the superexchange interaction of short-range exciton coupling. The hypersensitivity of the electron and hole transfer integrals to chromophore displacements implies that the formation of charge-transfer states originating from the perylene core is strongly dependent on stacking profiles. This effect causes aggregates with similar absorption spectra and dimer arrangements to exhibit a wide range of colors, a phenomenon known as crystallochromy.[73] This topic has been discussed elsewhere in detail.[44,74,75]

The degree of H-type aggregation can be measured by the ratio of the 0–0/0–1 vibronic peak intensities, which decreases in H-aggregates. Exemplary absorption spectra of PDI aggregate formation are shown in Fig. 3B. As PDI concentration increases, the ratio of the 0–0/0–1 absorption peaks decreases due to the formation of H-aggregates (Fig. 3B inset).[76] Fluorescence quenching in PDI aggregates is also explained by Kasha theory. Wavefunction overlap between core-localized HOMOs and LUMOs of adjacent chromophores facilitates the dissociation of the S_1 state into non-emissive charge transfer (CT) states, which are composed of a pair of charge carriers localized to adjacent chromophores. CT states are non-emissive, resulting in luminescence and phosphorescence quenching, and PDI

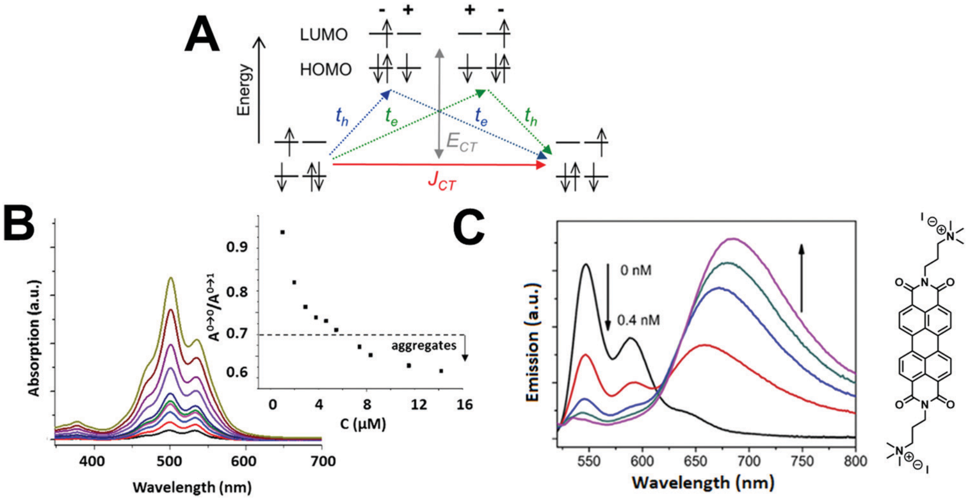

Fig. 3 (A) Energy level diagram of charge-transfer coupled chromophores. Reprinted with permission from ref. 75. Copyright 2017 American Chemical Society. (B) Prototypical concentration-dependent (1–14 μM) absorption spectra of a PDI in water exhibiting H-type aggregate formation. Peak area ratios of the 0–0/0–1 vibronic peaks are shown in the inset. Reprinted with permission from ref. 76. Copyright 2017 Elsevier. (C) Emission spectra of QA-I (right) titrated with 0–0.4 nM Ag nanoparticles. The nanoparticles induce PDI excimer formation at elevated concentrations. Reprinted with permission from ref. 80. Copyright 2018 Elsevier.

fluorescence can be tuned by orthogonal solvent blending.[77,78] CT formation is possible because the binding energy of the lowest charge transfer state is high in comparison with the valence and conduction bandwidths.[79] However, a number of $S_1 \rightarrow S_0$ relaxation pathways are possible in PDI aggregates. For example, excimers form when the S_1 excited state creates an internal electric field that causes the spacing between the chromophores to decrease or for the displacement of the chromophores to change such that the degree of wavefunction overlap increases between the neighboring species. The resulting state is lower in energy, causing the photoluminescence to dramatically red shift, accompanied by an increase in the exciton lifetime. The transformation from the monomer emission at 545 nm to excimer emission at 685 nm is shown in Fig. 3C. Here, Li *et al.* titrated a 0.1 μM solution of QA-I (Fig. 3C) with 0.4 nM of 30 nm silver nanoparticles. The monomer emission is quenched by >90% with an excimer/monomer emission intensity ratio of ~11.[80] This and other relaxation pathways are thus exploitable in PDIs for sensing applications.

3. Amine/ammonium functionalized PDIs (N-PDIs)

3.1 Physical properties

The properties outlined in the previous section still hold true for N-PDIs, though with a new layer of added complexity. Electron-rich amine and ammonium moieties are capable of doping the electron-poor dicarboxylic acid imides of PDI and have led to the material classification as self-n-doping.[81] However, many examples of N-PDIs in the literature have incorporated these moieties into the PDI scaffold to improve solubility in polar solvents.[82–86] The aggregation dynamics of N-PDIs appear to be highly sensitive to solvent polarity, and their solubility properties tend to vary with dopant architecture. This feature allows their fluorescence properties to be manipulated by solvent blending.[87] Their propensity for fluorescence quenching in polar solvents and blends makes them excellent sensors for a wide breadth of analytes using various optical techniques.[88–100] Self-assembly of N-PDIs has also been studied extensively, with aggregation into supramolecular structures being controlled with temperature differences, pH adjustment, metallic directing groups, and structural modifications.[101–110] Many of these phenomena have been reviewed elsewhere.[111] Additionally, many N-PDIs are amphiphilic mesogens capable of forming lyotropic liquid crystal mesophases and have been investigated for use in optical applications.[112–121]

3.2 Self-n-doping mechanism

Due to the unfavorable energy level alignment between the amine/ammonium dopants and the LUMO of PDI, self-n-doping proceeds through a photoinduced electron transfer mechanism. A graphical depiction of the doping mechanism is outlined in Fig. 4A. First, ground state PDI $^{0}\mathbf{N}$ undergoes photoactivation to produce the excited singlet state $^{1*}\mathbf{N}$. Here, $^{1*}\mathbf{N}$ can either relax back to the ground state or undergo reductive quenching by the amino donor to generate the radical anion ($\mathbf{R}^{\bullet-}$).[122–124] Doping can also be thermally activated in the solid-state. Reilly *et al.* fabricated thin films of the trimethylammonium hydroxide doped PDI shown in Fig. 4B. Upon heating to 120 °C for 20 minutes in air, the color of the films changed from a deep red to blue (Fig. 4B inset), and the film conductivity increased by nearly five orders of magnitude. The absorption spectra of the films show the conversion of the neutral species (**4B$_1$**) to the radical anion (**4B$_2$**). After sitting in air for 10 minutes (**4B$_3$**) and ultimately one day (**4B$_4$**), the radical is gradually oxidized back to the neutral species. Note that the absorption spectrum of an electrochemically generated

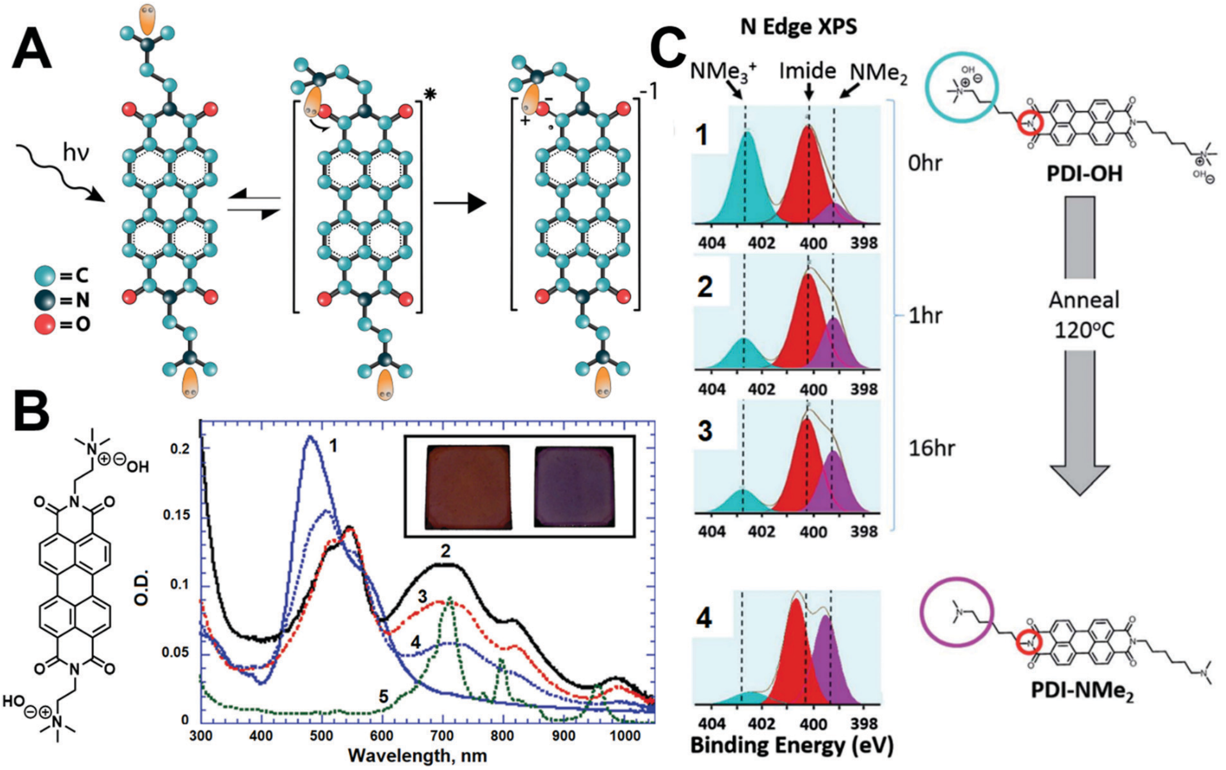

Fig. 4 (A) A graphical representation of the self-n-doping mechanism. (B) Chemical structure of the compound analyzed in the accompanying absorption spectrum. The numbered spectra correspond to the absorption of the (1) as cast; (2) after heating at 120 °C for 20 min in air; (3) 10 min after exposure to ∼33% humidity air; (4) 24 h in ambient air; (5) electrochemically generated radical anion in THF. Inset: As-cast film (left) and heated film (right). Adapted with permission from ref. 55. Copyright 2012 John Wiley & Sons Inc. (C) N 1s XPS spectra of an N-PDI (PDI-OH) before (1) and after heating at 120 °C for 1 h (2) and 16 h (3), as well as the N 1s XPS spectrum of the (PDI-NMe_2) for reference (4). The relative peak ratios of NMe_3^+, imide, and NMe_2 are shown in blue, red, and purple, respectively. Adapted with permission from ref. 127. Copyright 2012 John Wiley & Sons Inc.

PDI radical anion is provided as a reference (**4B$_5$**). The researchers also noted that similar changes in the absorption spectrum were observed when leaving the film in a moisture-free desiccator, indicating oxygen is the primary oxidant of the radicals.[122,125,126] Films of these N-PDIs with hydroxide, iodide, and chloride counterions were all found to have higher electrical conductivities after thermal annealing. Work functions of the films were tested with Kelvin probe measurements, finding that the as-cast film has a work function of 4.70 eV. Given a conduction band edge of ∼3.9 eV, they concluded that the as-cast films are weakly n-doped. After leaving them in a moisture-free environment for 12 hours, the work function shifted to 4.20 eV indicative of photoactivated doping from ambient light in the laboratory. Following thermal annealing, the work function shifted very near the conduction band edge to 3.96 eV. Additionally, thermogravimetric analysis revealed a ∼5% mass loss when annealing from 0 °C → 150 °C, which the authors attributed to water loss, implicating a solvent effect discussed in more detail below.[55]

Direct thermal activation of dopants is not possible. Russ *et al.* estimated the free energy change for charge transfer ΔG_{CT} from an amine donor to a neutral PDI acceptor to be ∼+1.4 eV in the solid-state, which is a barrier that far exceeds the ∼25–40 meV thermal excitation present when annealing samples, leading them to propose a secondary pathway involving sample decomposition. To support this, they monitored the stability of an ammonium salt dopant with X-ray photoelectron spectroscopy (XPS) of the nitrogen 1s region, whose structure and spectra are shown in Fig. 4C. Four peaks for the N 1s are observed for the as-cast film, assigned to the quaternary (blue) and tertiary (purple) nitrogen, as well as the imide (red) nitrogen. Upon heating to 120 °C, the quaternary ammonium fraction diminishes as the tertiary amine fraction increases, while the internal control imide nitrogen fraction remains unchanged, implicating a decomposition process. Mass spectrometry revealed a loss of 15 mass units, consistent with the loss of a methyl group. Fourier transform infrared spectroscopy revealed the loss of the broad OH stretching mode centered at ∼3400 cm^{-1}, consistent with water loss. Thus the quaternary ammonium deaminated to the tertiary amine with increasing annealing time. At the same time, electron paramagnetic resonance (EPR) showed an increase in spin concentration with annealing, consistent with electronic doping. However, the authors noted this transformation was not observed for samples with other counterions and appeared to be unique to the ammonium dopant when paired with a hydroxide counterion.[127] In testing a series of N-PDIs, we have similarly identified numerous examples of dopants that both do and do

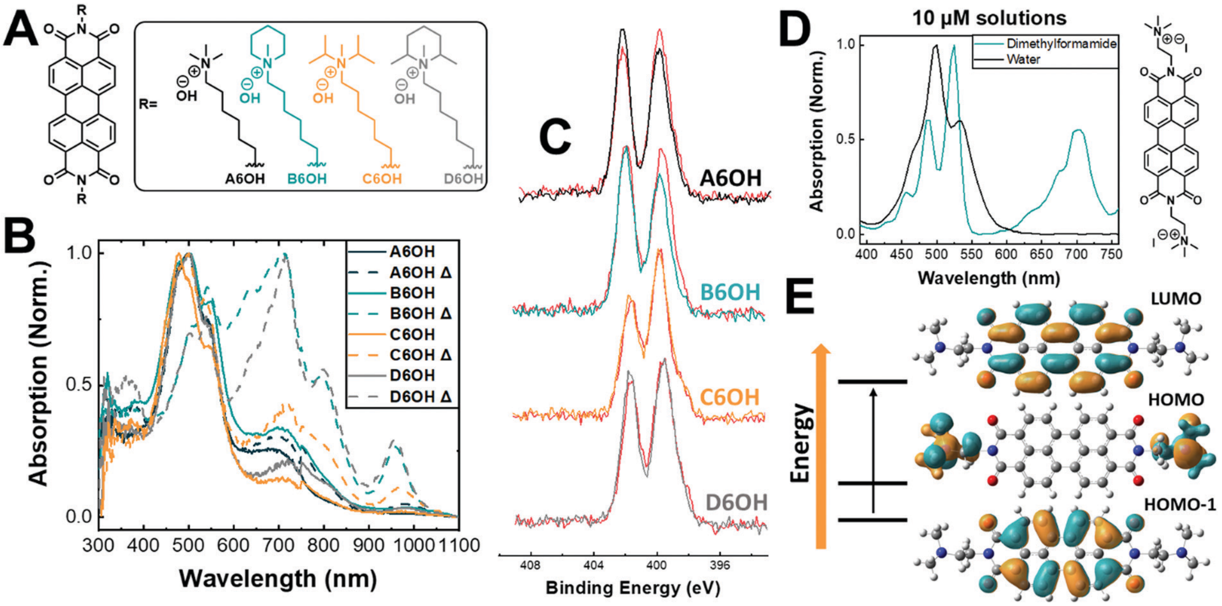

Fig. 5 (A) Chemical structures of A6OH, B6OH, C6OH, and D6OH. (B) Absorption spectra of thin films of each compound are presented in A before and after thermal annealing at 120 °C for 1 h in an inert atmosphere (annealed films are designated with a Δ symbol). (C) XPS spectra of the N 1s region of each compound before and after thermal annealing for 1 h in an inert atmosphere. Annealed samples are shown in red. (D) Absorption spectra of 10 μM solutions of A2I (structure shown) in DMF and water. (E) HOMO and LUMO Gaussian simulations of *N*,*N′*-bis[2-(dimethylamino)ethyl]3,4,9,10-perylenetetracarboxylic diimide computed at the DFT level using the B3LYP functional and a 6-311G** basis set, and accompanying transition energy diagram.

not degrade yet still show a marked increase in electronic doping even when degradation does not occur. Chemical structures for a selection of these compounds are shown in Fig. 5A. Absorption spectra for these compounds collected before and after thermal annealing at 120 °C under an inert atmosphere are shown in Fig. 5B, which shows the conversion of the ground state species (415–570 nm) to the radical anion (570–1100 nm) following annealing. Doping occurs for all compounds in this series following thermal annealing and is most pronounced in B6OH and D6OH. XPS spectra of the nitrogen edge collected before and after annealing are shown in Fig. 5C. Both A6OH and B6OH show signs of amine degradation, but C6OH and D6OH are stable.

Matsunaga *et al.* similarly found examples of structurally stable self-n-doping naphthalene diimides following photoactivation.[123] Degradation is thus an intrinsic property to the structural motif of the dopant in question, with certain structures being more prone to dealkylation. Instead of degradation, the increase in doping observed upon annealing is related to the residual presence of solvent. Absorption spectra of A2I measured in both DMF and water are shown in Fig. 5D. In water, the PDIs form H-aggregates and all remain in their neutral state. In DMF, monomers are present and radical anions easily form, as evidenced by the characteristic radical peak at 700 nm. Wang *et al.* similarly observed solvent selection during thin film processing affected radical anion formation. Methanol residue completely suppressed radical anion formation, while methanol/water mixtures favored radical anion formation following annealing.[128] Additionally, thermal activation may reduce the energy gap between the HOMO and HOMO−1, shown in Fig. 5E to promote photoinduced electron transfer. However, more work is needed to test this hypothesis.

3.3 Structure-function relationships

A number of structure-function relationships have been identified in N-PDIs. Perhaps the most dramatic effects come from the location of the dopants. Dopants can be bound directly to the PDI scaffold through covalent modification of two primary sites, namely the imides and the aromatic bay carbons. The choice of attachment mode affects the self-n-doping process in differing ways. This is because a transverse node in the HOMO and LUMO orbitals of the PDI core, as shown in Fig. 2C, electrically isolates the dopants when they are attached to the imides. Here, the HOMO is localized to the dopant, and the HOMO−1 → LUMO transition is equivalent to the HOMO → LUMO transition in un-doped PDIs. The arrangement of orbital energies shown here makes electron transfer ideal from the dopant to PDI following photoexcitation. The perylene core is an acceptor–donor–acceptor (A–D–A) system, and functionalization of the imides creates an electrically isolated D–A–D–A–D system. Doping, therefore, depends on the arrangements of the dopants relative to the core. Free rotation of the alkyl linkers is important for the donor to come into close proximity with the dicarboxylic acid imide acceptor and initiate electron transfer. Their electrical isolation also means the redox properties of the core are generally unaffected when dopants are attached to the imide nitrogens.

Photogenerated radical anions also form in N-PDIs functionalized at the core.[129–131] Zhao and Wasielewski investigated the redox properties of various core functionalized N-PDIs, as

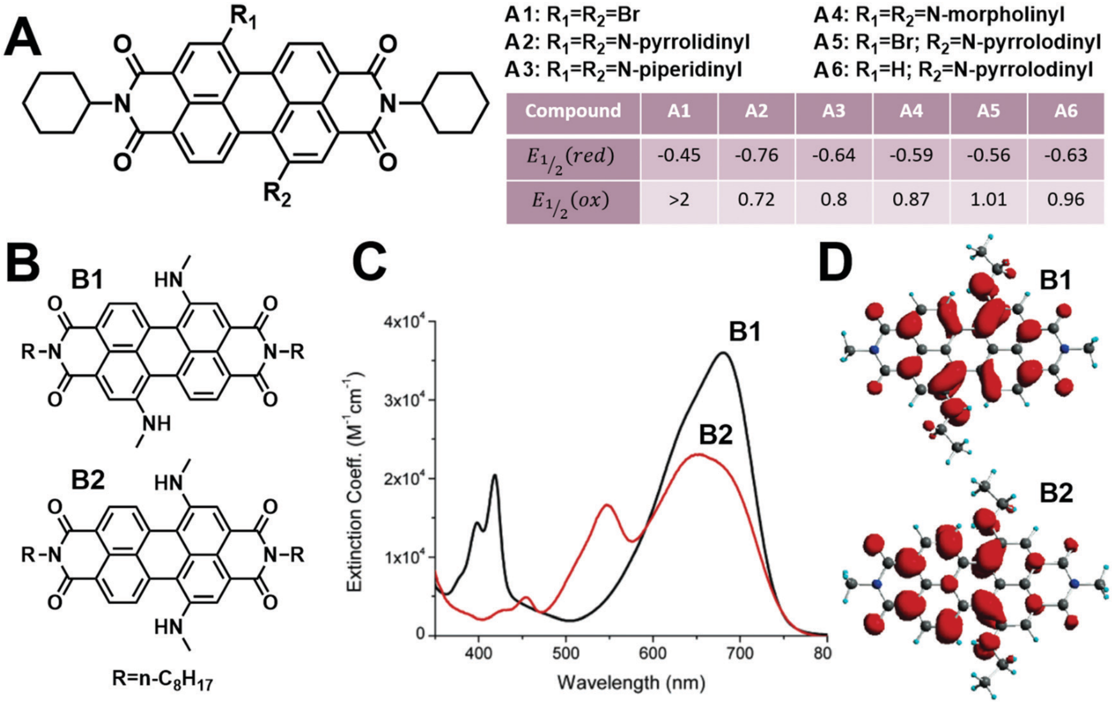

Compound	A1	A2	A3	A4	A5	A6
$E_{1/2}(red)$	-0.45	-0.76	-0.64	-0.59	-0.56	-0.63
$E_{1/2}(ox)$	>2	0.72	0.8	0.87	1.01	0.96

Fig. 6 (A) Chemical structures of compounds **A1–A6** and a table of redox potentials for each. (B) Structures of compounds **B1** and **B2**. (C) Absorption spectra of **B1** and **B2**. (D) Total spin density maps or geometry optimized **B1** and **B2**. Reprinted with permission from ref. 135. Copyright 2006 American Chemical Society.

shown in Fig. 6A, accompanied by their relative redox potentials. The addition of dopants resulted in a relatively modest negative shift in reduction potential by 0.3 V, compared to a pronounced negative shift in the oxidation potential up to 1.2 V *vs.* SCE. This dramatic shift in oxidation potential equates to a raised HOMO relative to vacuum and smaller bandgap, opening an exciting avenue to energy level alignment tailoring for device applications.[132] This notion is further supported by computational work by Langhals and Blanke, showing core functionalization dramatically raises the HOMO level relative to vacuum and subsequently lowers the barrier to self-doping.[133] The ability to modulate the HOMO is directly a result of the nodal pattern of the core, which causes moieties attached to the bay positions to be in direct electrical contact with these orbitals in a manner similar to that of push-pull systems.[134]

Ahrens *et al.* studied the dramatic bathochromic shifting that he and others have observed in the optical spectra of core-substituted N-PDIs. Compounds **B1** and **B2** shown in Fig. 6B are highly soluble in several solvents up to ~1 mM. Absorption spectra of **B1** and **B2** are shown in Fig. 6C, which are red shifted compared to imide substituted N-PDIs with a broad absorption band from 550–750 nm for **B1** and 475–750 nm for **B2**. The fluorescence of **B1** and **B2** are also strongly quenched for both compounds due to the presence of radicals which were measured with EPR. Thus, the core functionalized PDIs also undergo an intramolecular doping mechanism, but one that does not depend on chain rotation. The electrical connection of the amino-functional groups to the perylene core permits strong doping of PDI monomers. The group also performed electron nuclear double resonance (ENDOR) and EPR spectroscopies on **B1** and **B2** after treatment with oxidative $NOSbF_6$ to form the radical cation. This was done to probe the electron density distribution and nature of the electron donating species. Total spin density maps for these compounds are shown in Fig. 6D. The largest hyperfine coupling constants measured were those of the amino protons and amino nitrogen atoms, demonstrating that the amine forms a cation radical during charge transfer to the perylene core. They also found that the radical cationic amines were remarkably stable, with 50–80% of the signal intensity decreasing after sitting in air for a week for **B1** and **B2**, respectively.[135]

Direct comparisons between core and imide functionalization were performed by Wu *et al.* who compared the photo-induced electron transfer of two PDIs functionalized at the imide position with that of one functionalized at the core (Fig. 7) using steady-state absorption and fluorescence spectroscopy in various polar organic solvents and two room-temperature ionic liquids (RTIL).[136] Absorption and emission properties are given in Table 1, where ε is the molar extinction coefficient, λ_a is the wavelength of the 0–0 absorption, λ_f is the wavelength of the 0–0 emission, and Φ_f is the fluorescence quantum yield. The absorption spectra of compounds **C1** and **C2** in all solvents exhibited absorption spectra characteristic of neutral monomers in solution. The absorption maximum of the 0–0 transition red-shifted up to 8 nm for **C1** and 6 nm for **C2**, depending on the solvent environment. The absorption spectrum of compound **C3** was similar to that of **B1** and **B2**, with a broad absorption band from 550–750 nm, and exhibited the

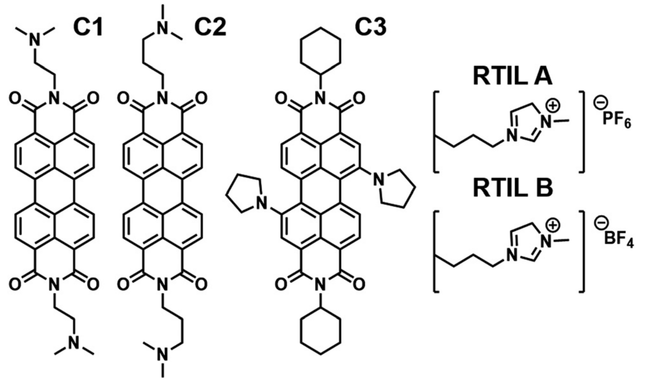

Fig. 7 Chemical structures of **C1–C3** as well as the structures of room-temperature ionic liquids (RTIL) A and B.

largest red shift up to 27 nm in different solvent environments. The authors attributed the red shifting to solvent stabilization of the polarized charge transfer states, which would be greatest in systems forming stable radical anions. The fluorescence quantum yields varied substantially for **C1** and **C2**, while **C3** remained fairly low in all solvents, ranging from 0.40% in RTIL A to 2.56% in toluene. The fluorescence was strongly quenched in the organic solvents, with **C1** and **C2**, respectively, exhibiting quantum yields of 1.60–5.90% and 1.97–5.36%. Surprisingly, the respective quantum yields for **C1** in RTIL A/B were 98.35% and 46.47%, and for **C2** 84.42% and 42.76%. The strong fluorescence quenching that Wu and coworkers observed is due to the presence of radicals, and demonstrates that solvent polarity can play a decisive role in the self-doping process for PDIs. Additionally, since the structures of **C1** and **C2** only differ by a single methylene tether between the donor and acceptor, the differences in quantum yields between these two species can be attributed to improved spatial conformation between the longer donor tertiary amine and acceptor core, which is consistent with similar intramolecular donor-acceptor systems.[86,137,138] This concept is further supported by fluorescence spectroscopy studies of PDIs substituted at both the core and imide positions with tertiary amines. The fluorescence quantum yields decrease much more dramatically with core substitution than imide substitution due to the non-emissive nature of CT states.[139,140]

Wang *et al.* compared differences between tertiary amine and quaternary ammonium self-dopants both with and without functionalization of the PDI core with electron-withdrawing and donating substituents. The structures for these compounds are shown in Fig. 8A. The general naming scheme is based on substituents added to the PDI core (R) and the substituents added to the imide positions (X) in the manner of P‘R’F–‘X’. For the range of core substituents in this study, R = H for hydrogen, R = C for chlorine, and R = O for *o*-methoxy-phenyl. In the case of the imide substituents, X = N for the tertiary amine, X = Cl for the ammonium chloride, X = OH for the ammonium hydroxide, X = BIm_4 for the ammonium tetrakis(1-imidazolyl)borate, and X = F for the ammonium fluoride functional group. The addition of electron-withdrawing chloro substituents changes the HOMO and LUMO energies in a manner opposite to that of the electron-donating *o*-methoxy-phenyl groups, as shown in Fig. 8B, and was confirmed by cyclic voltammetry to have a ~0.2 eV gradient. The authors compared the impact of these structural and phase-dependent changes on the self-doping process *via* absorption spectroscopy studies. The absorption spectra of the samples in methanol are shown in Fig. 9A–C. The set of neutral S_0–S_1 peaks is slightly red-shifted between the PHF–X, PCF–X, and POF–X samples due to small changes in the HOMO energy by core substituent addition. Interestingly, all of the chloro-substituted samples show electronic doping in the ~600–1100 nm region with the exception of PCF–Cl. As thin films, the PHF–X samples exhibit relatively low doping density, while doping is not observed in the POF–X samples (Fig. 9D–F) and is most significant in the PCF–X samples. Thermal annealing also enhances doping density in these samples and is necessary for the PHF–X samples to show an appreciable degree of doping (Fig. 9G–I). The samples most sensitive to annealing were PCF–F and PCF–BIm_4 upon thermal annealing, though the absorption intensities increased for all PCF–X samples. These findings implicate interesting ways of modifying self-dopant efficiency through core functionalization, as well as the ability of counterions to affect the formation of radical anions.[128]

Table 1 Absorption and emission spectral parameters of **C1–C3** in various solvents

Compounds		RTIL A	RTIL B	DMF	THF	CH_2Cl_2	Toluene
C1	$\varepsilon \times 10^4$ (mol^{-1} L cm^{-1})	8.77	8.73	8.74	8.20	8.70	8.33
	λ_a (nm)	524	527	524	518	520	526
	λ_f (nm)	539	543	539	534	536	541
	Φ_f (nm)	98.35	46.47	1.60	2.15	2.26	5.90
C2	$\varepsilon \times 10^4$ (mol^{-1} L cm^{-1})	8.46	8.26	8.62	8.65	8.54	8.66
	λ_a (nm)	524	526	524	520	523	526
	λ_f (nm)	540	542	540	533	537	540
	Φ_f (nm)	84.42	42.76	1.97	2.54	3.16	5.36
C3	$\varepsilon \times 10^4$ (mol^{-1} L cm^{-1})	4.64	4.70	4.49	4.73	5.02	4.80
	λ_a (nm)	712	713	701	685	699	686
	λ_f (nm)	754	756	748	723	734	717
	Φ_f (nm)	0.40	0.33	0.62	1.63	1.60	2.56

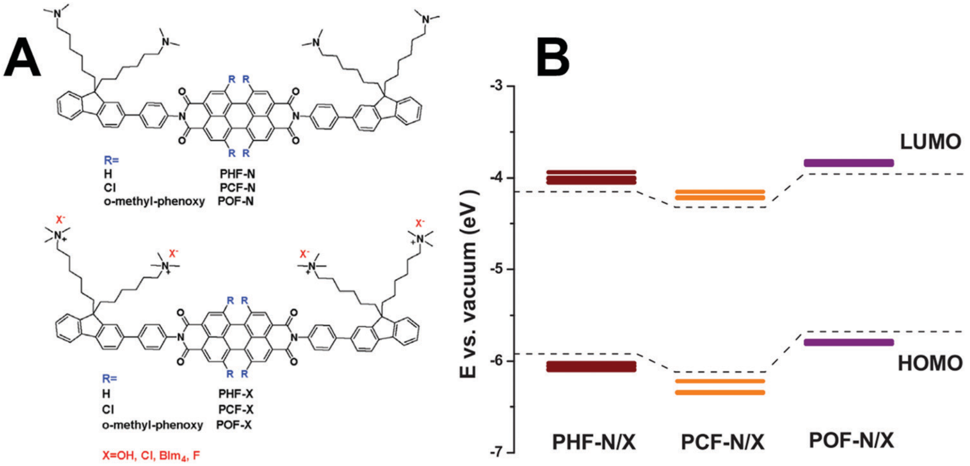

Fig. 8 (A) Chemical structures of P'R'F–'X' derivatives, where R corresponds to bay functionalization with hydrogen, chlorine, or *o*-methyl-phenoxy, and X corresponds to the anionic counterion in quaternary ammonium structures, where OH is hydroxyl, Cl chloride, $\mathrm{BIm_4}$ is tetrakis(1-imidazolyl)borate, and F is fluoride. (B) Relative changes to the HOMO/LUMO levels when the PDI core is functionalized with hydrogen, chlorine, or *o*-methyl-phenoxy in PHF–X, PCF–X, and POF–X, respectively. Reprinted with permission from ref. 128. Copyright 2017 John Wiley & Sons Inc.

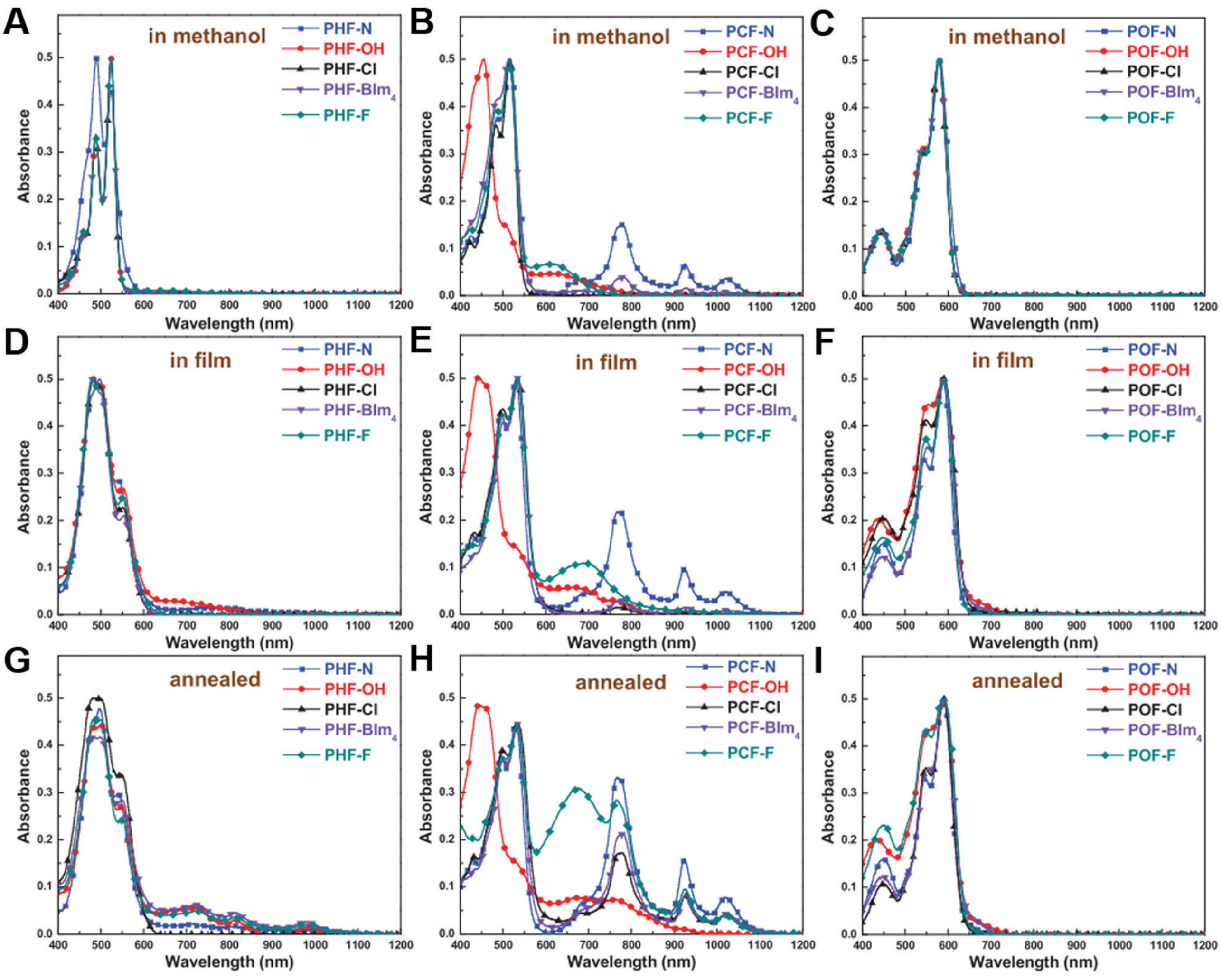

Fig. 9 Absorption spectra of P'R'F–'X' derivatives (A–C) in methanol, (D–F) as cast in thin films, and (G–I) after annealing at 85 °C for 20 min. Reprinted with permission from ref. 128. Copyright 2017 John Wiley & Sons Inc.

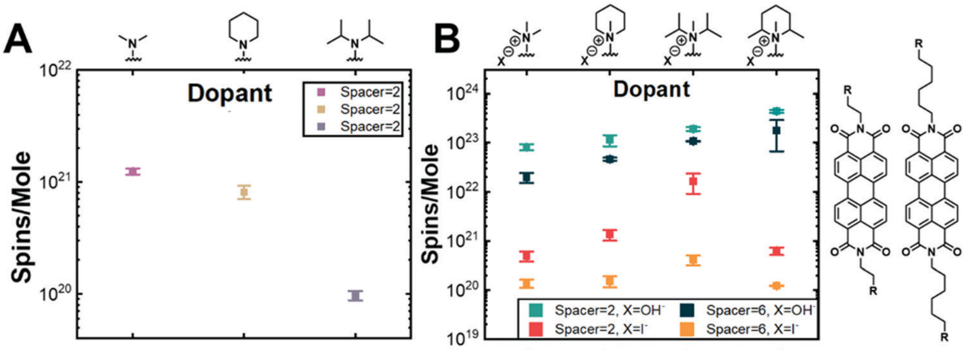

Fig. 10 (A) Quantitative EPR measurements of spin concentration for tertiary amino doped N-PDIs with increasing steric encumbrance. (B) Quantitative EPR of sterically encumbered ammonium doped N-PDIs. The groups vary by steric encumbrance, tether length, and counterion.

Our work has attempted to address dopant design principles in N-PDIs, which had been previously lacking.[141] We investigated the effect of steric encumbrance on the performance of tertiary amino dopants, whose structures are shown in Fig. 10. The dopants were attached to PDI at the imides with a two-carbon tether. Quantitative EPR measurements of these samples showed that more steric encumbrance decreases the efficiency of dopants in tertiary amines due to the obstruction of the nitrogen lone pair's electron donating ability, as shown in Fig. 10A. Interestingly, the more encumbered dopants also exhibit greater air stability, which we hypothesize is a result of the protection of the carriers from oxygen by the bulky groups. The opposite trend was observed in samples doped with quaternary ammonium moieties, whose structures are shown in Fig. 10B. The structures vary by tether length (two and six-carbon tethers), counterion (iodide and hydroxide), and steric profile. Quantitative EPR of these samples reveals that steric encumbrance increases doping efficiency, as shown in Fig. 10B. We rationalize this opposing trend by noting that the inclusion of steric bulk weakens the interaction of the anion with cationic nitrogen, which leads to an overall increase in Lewis basicity of the anion, thereby improving doping efficiency.

Steric encumbrance also plays an essential role in the solution phase. N-PDIs with two carbon tethers were diluted to 10–60 μM in dimethylformamide in the dark, sealed in anaerobic cuvettes under an inert atmosphere, and their absorption spectra were measured. Absorption spectra for the two N-PDIs with the least steric encumbrance and an iodide counterion are shown in Fig. 11A and hydroxide counterion in Fig. 11B. In the samples with iodide counterions, all PDIs are in the neutral state. In contrast, the samples with hydroxide counterions exhibit a high degree of electronic doping such that all of the neutral species have been converted to either the radical anion (∼600–1000 nm) or the dianion (∼500–600 nm).

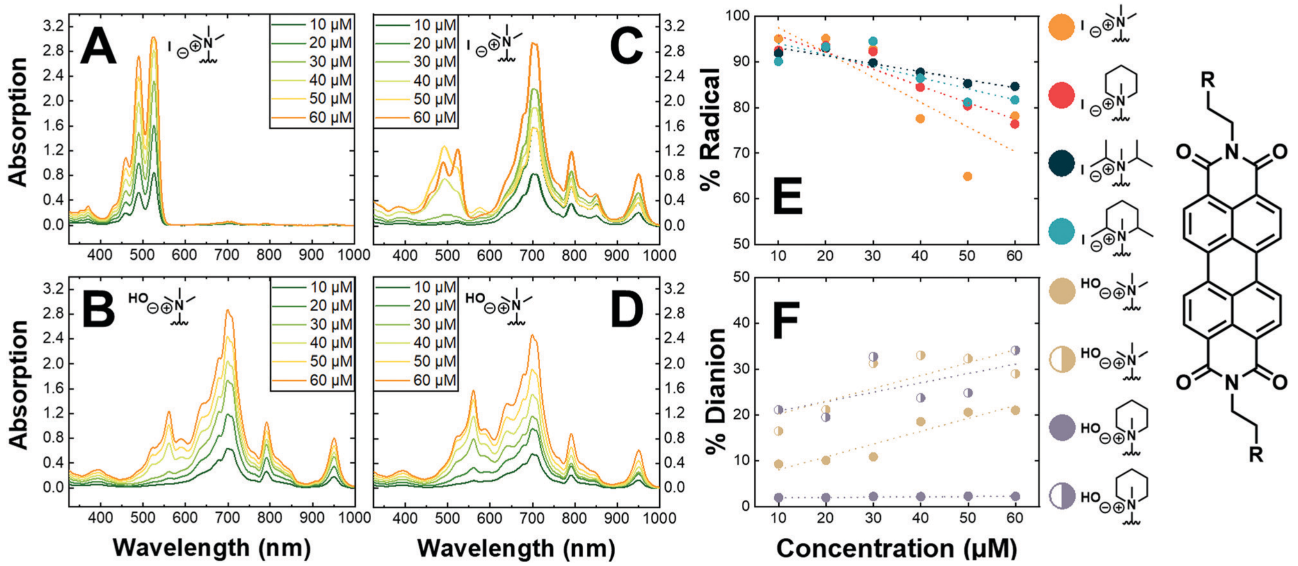

Fig. 11 (A and B) Absorption spectra of N-PDIs (structures in insets) measured in the dark at 10–60 μM in sealed anaerobic cuvettes. (C and D) The same samples in A and B after 90 minutes of irradiation with a 405 nm lamp. Samples remained sealed in the cuvettes throughout the experiment. (E) Percentage radical anion formation for four samples (structures to the right) before and after irradiation at 10–60 μM concentrations. (F) Percentage dianion formation before (filled) and after (half-filled) photoirradiation of two N-PDIs (structures to the right). Adapted with permission from ref. 143. Copyright 2022 American Chemical Society.

Thus, the hydroxide is a much stronger dopant than iodide, which generally follows Lewis basicity trends. Samples were then irradiated with a 405 nm lamp for 90 minutes and measured once again. Fig. 11C and D shows the increase in radical anion concentration upon photoirradiation. The percentage difference between the integrated intensity of the neutral and radical anion spectra for the iodide samples measured in the dark and after irradiation were calculated and plotted in Fig. 11E. It can be seen from this plot that radical anion formation is most efficient in the low concentration regime. As the concentration increases, the dopants are less free to tumble in solution, and chain rotation is inhibited, leading to a decrease in radical formation. Interestingly, the opposite trend was found for dianion formation. As shown in Fig. 11F, dianions form much more readily in the high concentration regime than at lower concentrations. Additionally, dianions do not form in systems with more sterically encumbered dopants. The dopant with the lowest degree of steric encumbrance had the highest concentration of dianions.[142] We hypothesize that dianions favor these conditions due to Coulombic stabilization of the charge between adjacent chromophores in a manner similar to that of exciton stabilization in PDI aggregates. Additionally, bulky dopants would inhibit interactions between neighboring chromophores and impair charge delocalization.

In view of these principles, one must take into careful consideration a number of parameters. First, the mode of attachment will strongly impact doping efficiency, with core attachment being generally favored. Electron withdrawing and donating groups attached to the core may also be used to alter doping efficiency. While clear in imide doped N-PDIs, it remains to be investigated how attachment distance affects doping efficiency in core doped N-PDIs. Additionally, the choice of architecture between amine and ammonium dopant will affect efficiency. In our own systems, we found that ammonium dopants are more effective than amines, but only when paired with strongly Lewis basic counterions. We also observed shorter tethers to be more effective at doping due to the closer proximity of the dopant to the acceptor, though it should be noted that there are instances of N-PDIs with longer tethers with much higher electrical conductivities.[81] This phenomenon may be morphologically driven, though, and therefore specific to these structures in particular rather than a general working design principle. On the other hand, charge separation could play a role that favors longer chains. Finally, the effect of steric encumbrance will depend on whether one uses tertiary amines or quaternary ammonium substituents and whether one is working in solution or the solid state, as there are trade-offs in each regime. Attaching self-dopants to PDIs adds rich complexity to the optical, electronic, and physical properties of these molecules, whose manifestation depends on the mode of attachment, attachment distance, and dopant structure. Changes to the native properties of PDIs, namely the presence of radical anions or dianions, HOMO/LUMO energy, absorption features, solubility, and conductivity are a direct consequence of the dopants.

4. Applications

4.1 Biochemistry

Perhaps the most widely investigated application of N-PDIs has been in biological environments. Ionic PDIs are naturally suited to biological applications due to their solubility in aqueous environments. The inclusion of water-soluble ammonium salts, coupled with PDI's innate photophysical properties and controllable self-assembly, has led to a number of interesting uses. Perhaps surprisingly, PDIs functionalized with amines have also been reported in a number of these roles, dispelling the notion that PDIs must contain an ammonium salt to serve any functional role in these environments.[143–147] N-PDIs are even amenable to the homochiral nature of biological environments. It has been shown that N-PDIs are capable of chiral self-assembly to form various structures such as supramolecular helices and can further be used as biologically-based chiral sensors.[148–153] For example, N-PDI's photoluminescence and electroluminescence properties can be tuned in both turn-on and turn-off sensing of various analytes such as nucleic acids, tumor markers, proteins, and drugs.[154–160]

The relationship between N-PDIs and DNA has been the subject of the most widespread investigation due to its role in disease and the emerging interest in using DNA as a molecular wire, data storage, and other electronics applications.[161–167] Manipulations of the DNA scaffold have long been a core component within the biochemistry field, leading to an exciting crossover between biological and semiconductor sciences. For example, work by T. Takada *et al.* has demonstrated that PDI coordinates within hydrophobic abasic cavities created within DNA strands, as shown in Fig. 12A and B.[47] When base pairs are removed from DNA strands containing a deoxyribose (dS_n) spacer, a corresponding number of cPDI chromophores ($P[n]$) coordinate in the formed pocket through hydrophobic interactions. By spacing apart the hydrophobic pockets (Fig. 12C), the authors were able to observe evidence of excitonic coupling between the chromophores using absorption spectroscopy. Fig. 12D shows the changes between the 0–0 and 0–1 peak ratios when the hydrophobic pocket sizes were increased (dS_n $1 \rightarrow 5$), as well as when the spacing between dS_2 hydrophobic pockets was increased. H-Type co-facial stacking was observed as more PDI chromophores aggregated within the increasingly larger dS_n cavities, while excitonic coupling between chromophore dimers sandwiched in dS_2 pockets resulted in a decrease in the absorbance intensity ratio A_{0-0}/A_{0-1}.[168]

Takada and coworkers have also investigated the photoconductivity of both sets of one-dimensional $P(n)$ nanoarrays. The interested reader is directed to an investigation of the photoconductivity and charge separation dynamics of the dS_2 systems.[169] As shown in Fig. 13A, PDI—DNA arrays are anchored to gold electrodes, and their photoconductivity responses are measured with a 540 nm excitation source. All complexes exhibit sharp on-off photocurrent responses (Fig. 13B) that increase by 4× (P2) and 8× (P3) upon subsequent addition of a single chromophore into the array; this despite virtually equivalent oscillator strengths of the 540 nm

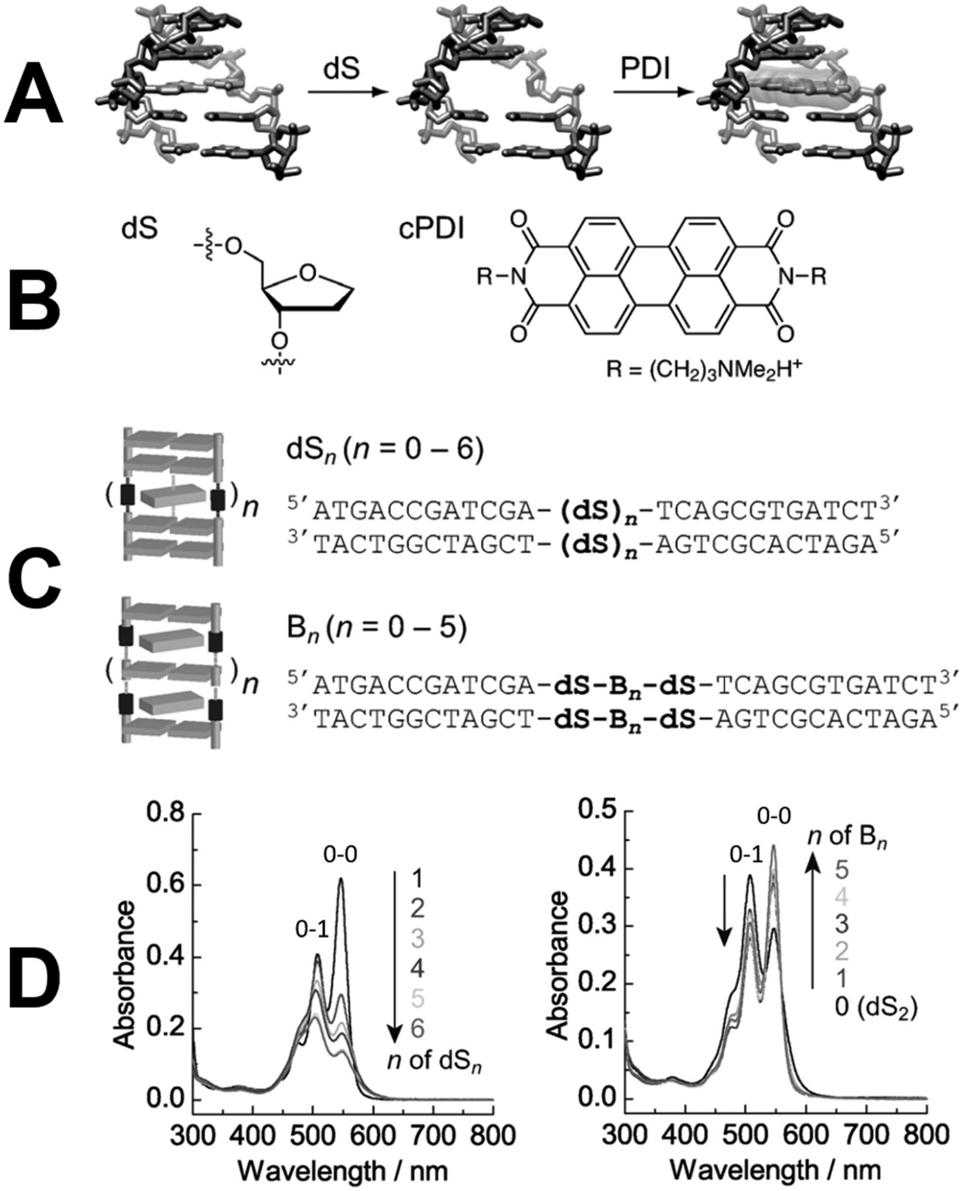

Fig. 12 (A) Representation of PDI coordinating to a hydrophobic pocket created within a DNA strand by replacing nucleosides with abasic analogues. (B) Structure of the abasic deoxyribose spacer (dS) and cPDI. (C) DNA sequences with different binding cavity configurations; the first with dS_n abasic sites and the second with B_n cavity spacers composed of alternating A–T pairs between two dS sites. (D) Absorption spectra of dS_n and B_n DNA configurations. Reprinted with permission from ref. 168. Copyright 2012 John Wiley & Sons Inc.

excitation for P1, P2, and P3. Fig. 13C displays the photocurrent action spectrum overlaid on the absorption spectrum of each complex. The photocurrent response at each excitation wavelength follows the absorption spectral features of the chromophores, indicating that the photocurrent response originates as a direct result of the PDI aggregate conformations. To explain the underlying mechanism, femtosecond time-resolved transient absorption measurements were carried out on the complex series. Ground state bleaching in Fig. 14A–C is observed for all complexes at around 540 nm, and the formation of a charge separated PDI radical anion at ~720 nm is produced in P1 by charge transfer from the adjacent adenine base to excited PDI, which results in a slight red-shift in the absorption feature. P2 and P3 both exhibit a broadening of this absorption feature ranging from ~575–775 nm, which the authors attribute to delocalization of charge along the PDI chromophores. The decay profiles of the 720 nm excitation in Fig. 14D have similar constants of 0.8 ns but with broadened biexponential tailing features related to the greater transient absorption intensities at 720 nm for the series, consistent with the formation of longer-lived charge delocalized states in PDI aggregates.[170]

The role of DNA is central to life and thus plays a critical role in the progression of many diseases, such as cancer. N-PDIs have demonstrated anti-cancer activity through selective inhibition of telomerase, the protein responsible for the seeming agelessness of cancer cells by lengthening telomere sequences.

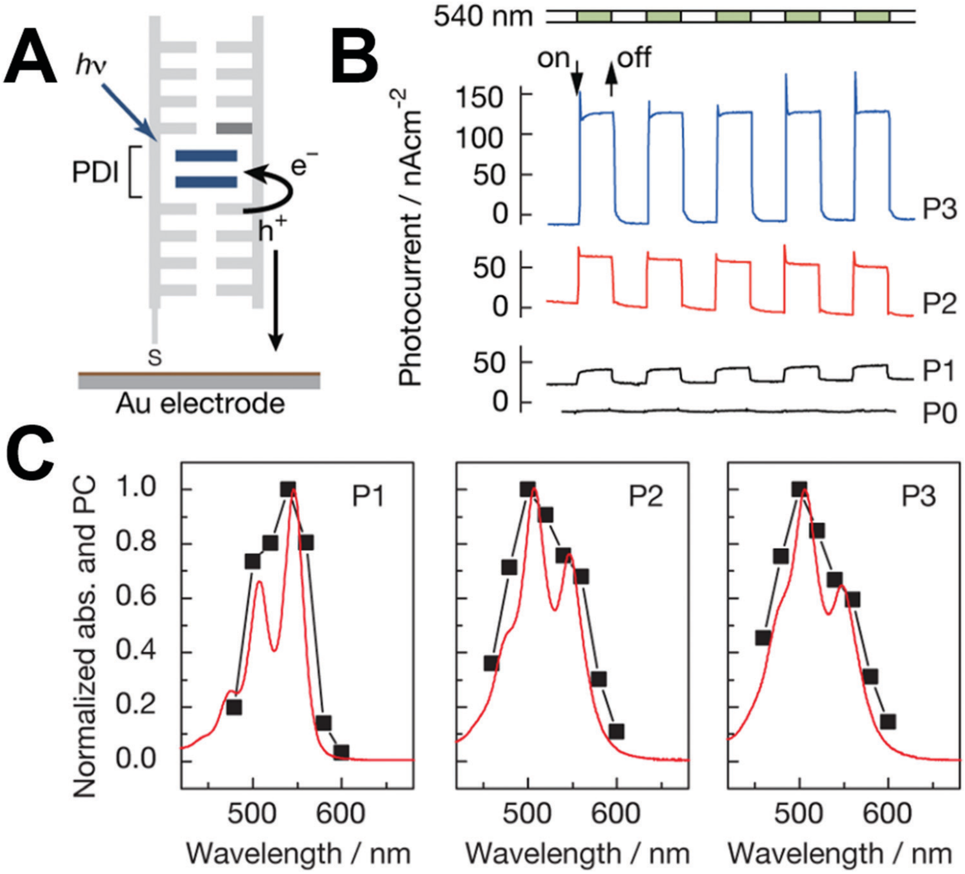

Fig. 13 (A) Schematic representation of photocurrent generation in a P2 complex (two cPDI units coordinated in a dS_2 pocket) bound to a gold electrode. (B) Photocurrent response to irradiation with a 540 nm excitation source with a 10 s repetition time in P_n complexes. (C) Action spectra of P_n complexes, displaying the normalized absorption spectra (red) and photocurrent (black). Reprinted with permission from ref. 170. Copyright 2014 American Chemical Society.

Indeed, ammonium substituted PDIs have been shown to have excellent cellular uptake.[171] A number of amine and ammonium functionalized PDI derivatives have been found to bind G-quadruplexes, supramolecular structures that form within telomeric and other oncogenic promoter sequences of DNA.[172–174] The binding has also been found to be pH dependent, with monomeric species binding in low pH environments to both DNA duplexes and G-quadruplexes and selective binding of G-quadruplexes with higher-order aggregation at higher pH.[175] Amino/ionic PDIs have been found to act as potent competitive binders to these DNA regions over telomerase and are highly selective to them over other double or single-stranded DNA sequences.[146] Interestingly, some of the most potent PDI inhibitors include multiple dimethylaminoethyl groups added to both the imides and core, such as DAPER4C(1,7), whose structure and binding to a monomeric G-quadruplex obtained by simulated annealing are given in Fig. 15A and B.[48] Similar work has been extended to other perylene and coronene derivatives.[176] Beyond *in vitro* telomerase inhibition, Xu *et al.* observe cytotoxic PDIs substituted with trimethylammonium functional groups inhibit the growth of HeLa and HCT116 cancer cell lines. Their family of PDIs specifically bioaccumulate within animal cell nuclei by intercalation and preferential interaction with DNA. They compared substitutions of up to six ammonium ion species with ionic strength, finding greater DNA intercalation in smaller, more strongly ionic species.[177,178]

DNA is central to cellular proliferation in bacterial infection. In compelling work, Jiao *et al.* found selective antibacterial action of a supramolecular N-PDI related complex. As shown in Fig. 15C, PPDI is complexed with two equivalents of the cucurbit[7]uril macrocycle (CB[7]) which encapsulate the phenyl end-groups creating barbell-like structures with a binding constant of 2.9×10^{12} M^{-2}, which is attributed to the interaction of CB[7] with both the phenyl and ammonium groups of the side chains. The complex effectively decreases aggregation of PPDI, as indicated by the oscillator strength of the 0–0 transition in the absorption during the titration of PPDI with CB[7]. The authors chemically reduced 0.3 mM solutions of both PPDI and PPDI/CB[7] complexes in water with $Na_2S_2O_4$ and found that PPDI/CB[7] is capable of bearing twice as many radicals as PPDI, as depicted in Fig. 15D. Quantitative EPR reveals the concentration of these radicals in solution to be 0.016 mM and 0.03 mM, equating to ∼5% and 10% doping,

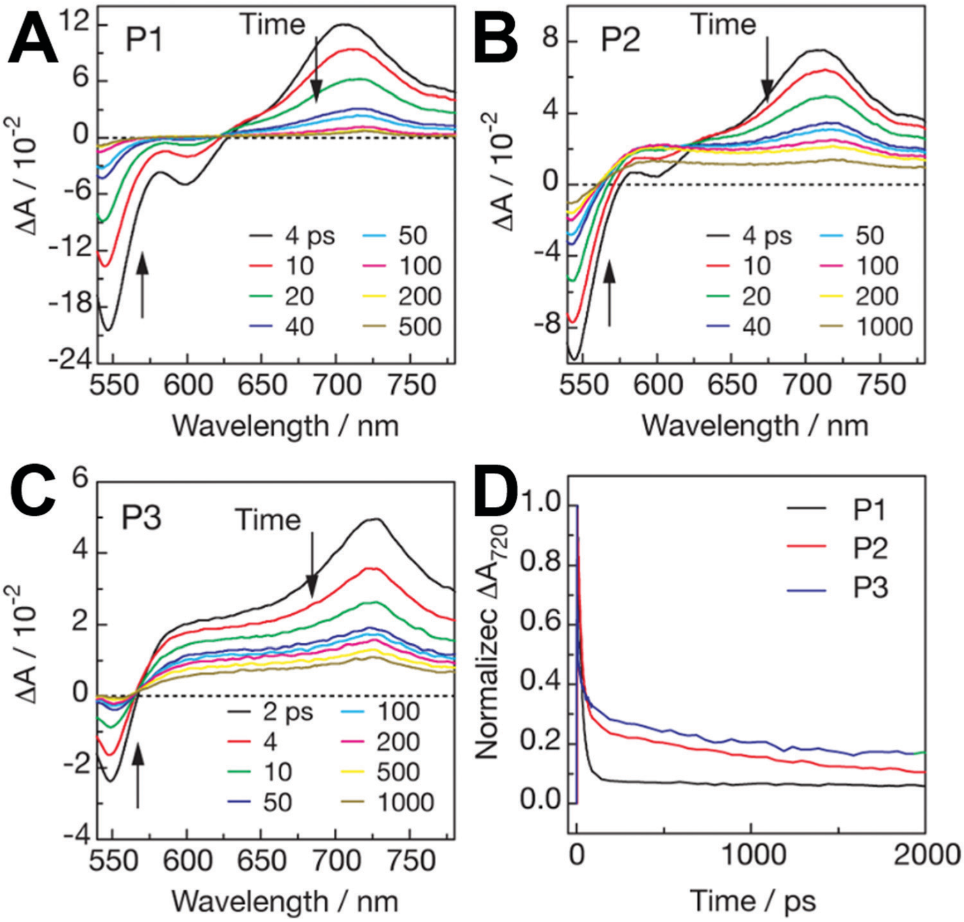

Fig. 14 Transient absorption spectra of (A) P1, (B) P2, and (C) P3 in a 20 mM pH = 7 sodium buffered solution using a 150 fs 540 nm excitation source. (D) Decay time of P_n complexes monitored at 720 nm. Reprinted with permission from ref. 170. Copyright 2014 American Chemical Society.

respectively. Interestingly, the radical yields for PPDI and PPDI/CB[7] are concentration-dependent, with more radicals populating the PDI scaffolds at higher concentrations. However, the rate of maximum radical anion yield increased more rapidly in PPDI/CB[7] complexes. Since the complexation depresses the formation of aggregates in solution, the authors concluded this to be the cause of higher radical yield in radical anion formation. The authors then performed photothermal conversion experiments, observing that irradiation with an 808 nm light with 1 W cm^{-2} power resulted in a much higher rate of water temperature increase, as well as higher overall water temperature, for the complexes in comparison with PPDI and the water control (Fig. 16A and B), and yielded roughly 2× the efficiency of conversion than that of PPDI.[179] Perylene diimides that form stable radical anions often exhibit enhanced performance as photothermal conversion materials,[180] and as such N-PDIs show great promise in cancer phototherapy applications.[181–183]

In subsequent work, various bacterial strain's ability to reduce PPDI/CB[7] complexes in lieu of added chemical reductant was tested. Radical anion formation is observed after incubation of PPDI/CB[7] with *E. coli* for 10 h. Interestingly, this effect is not observed for other bacterial strains, such as *B. subtilis* and *P. aeruginosa*. Additionally, other strains produce the effect, including *E. faecalis* and *S. aureus*, each with varying degrees of radical anion being generated. Photothermal conversion treatment in aqueous media was performed on *E. coli* and *B. subtilis* strains for their respective strong and nonexistent radical formation. Fig. 16C–E displays thermal imaging of the irradiated samples using the same procedure as in the previous study. While the *B. subtilis* samples do not show a temperature change, *E. coli* samples rose to 65 °C in 30 minutes. Other cell lines were also tested, and their radical formation response was measured with electron paramagnetic resonance, shown in Fig. 16F. The authors hypothesize that the presence of bacterial hydrogenases is responsible for radical formation, and thus the therapy could be used for bacterial strains possessing strong reductive capabilities. Bioaccumulation of PPDI/CB[7] in both *E. coli* and *B. subtilis* was verified with confocal laser scanning microscopy to ensure that the effect was not a product of accumulation. In terms of cytotoxicity, the authors found that PPDI inhibited the growth of both *B. subtilis* and *E. coli* bacteria, while PPDI/CB[7] permitted their growth, and also showed no clear cytotoxicity toward the nonmalignant HaCaT epithelial cell lines, indicating that these

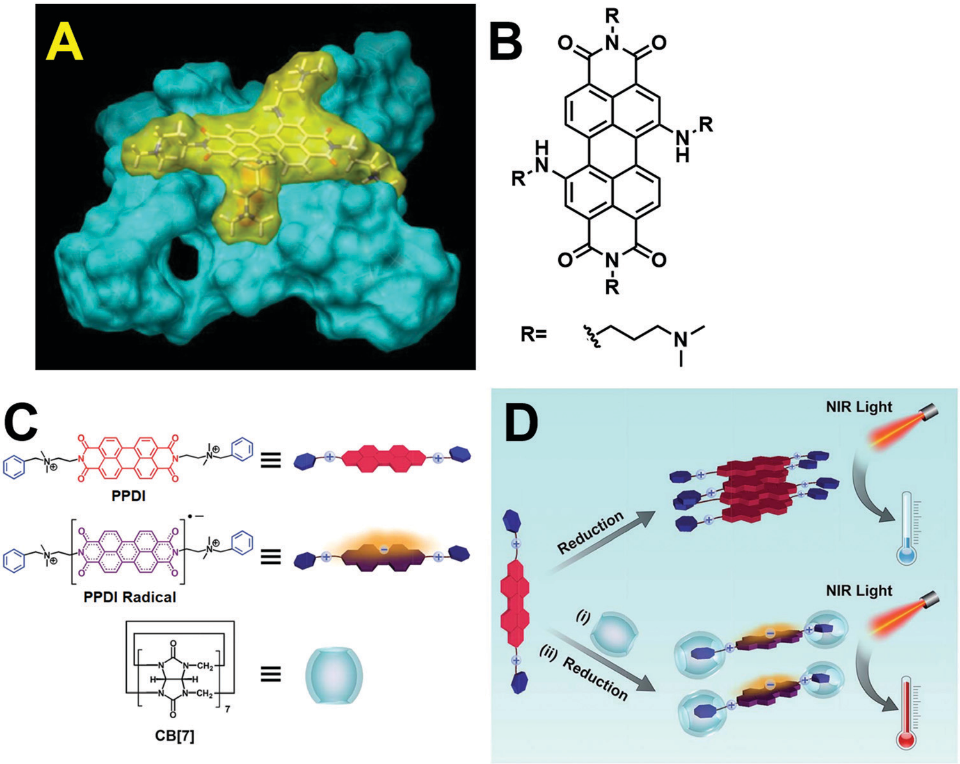

Fig. 15 (A) Molecular modeling simulation of DAPER4C(1,7), shown in (B) and depicted in yellow, bound to a monomeric G-quadruplex shown in blue. Adapted with permission from ref. 49. Copyright 2007 Elsevier. (C) Structures and schematic depictions of PPDI, PPDI radical anion, and CB[7]. (D) BPDI radical anions generated by reduction with sodium dithionate yielding low NIR photothermal conversion efficiency (top); formation of a BPDI/(CB[7])$_2$ supramolecular complex between, which was reduced with sodium dithionate yielding improved NIR photothermal conversion efficiency (bottom). Reprinted with permission from ref. 179. Copyright 2015 John Wiley & Sons Inc.

materials could be used in selective photoconversion therapies.[184] The interested reader is also directed to a study where these complexes are used in analyte sensing.[185]

4.2 Solar energy

Energy consumption across the globe is expected to increase by ~50% by 2050, and currently, the vast majority of energy comes from fossil fuels. Renewables are also the fastest-growing energy utility in the US, and solar is projected to surpass wind energy in becoming the dominant source of renewable electricity generation in the U.S. by 2040; the generating capacity of solar across all sectors is expected to grow by more than 5× its current capacity by 2050. Additionally, major production of solar materials has driven down costs by more than 100 times the cost per watt in the 1960s.[186,187] Bulk heterojunction organic photovoltaics (BHJ-OPVs) are solution-processable and synthetically modular, making them highly attractive as next-generation solar cell devices.[188] Electron transporting layers (ETL) and cathode interlayers are important in BHJ photovoltaics because they help minimize energy losses at the layer interfaces. A diverse range of self-n-doped materials have been reported as efficient ETLs and cathode interlayers in solar cells, some with benchmark performances.[22–24,31,189–194] Numerous examples were recently reviewed elsewhere in excellent detail.[195] N-PDIs have been shown to increase the broadband absorption of active layers, improve ETL homogeneity, and enhance solvent orthogonality for improved processability of BHJs.[196,197] In BHJ-OPV devices, N-PDIs also act as effective ETLs due to their energy level alignment and self-doping character.[198,199] For example, the power conversion efficiency of an (ITO)/PEDOT:PSS/PTB7-Th:PC71BM/ETL/Ag solar cell device that incorporates an N-PDI as an ETL increases from 5.61% (no ETL) up to 10.06%.[128] Various structures may be imagined for N-PDIs as ETLs. Zwitterionic structures show improved solar cell performance in fully organic BHJ devices, achieving power conversion efficiency values up to 11.23%. Additionally, when compared directly with tertiary amines, the zwitterionic N-PDIs outperform other structures through improved surface wettability during fabrication.[200–204]

Hybrid perovskite solar cell research has flourished in the last decade and garnered widespread attention from the materials community. N-PDIs have demonstrated superior performance in hybrid perovskite solar cells over some common ETL alternatives. Min *et al.* compared ZnO and PDINO ETLs in mixed halide p–i–n device stacks shown in Fig. 17A. Without an ETL, the maximum power conversion efficiency (PCE) is 10%. Incorporation of ZnO improves the PCE by 11.3%, while devices utilizing PDINO as the ETL reach a maximum PCE of 14.0%. The fill factors of the devices linearly increase from the control to ZnO and PDINO devices by 67.6, 47.5, and 78.5%,

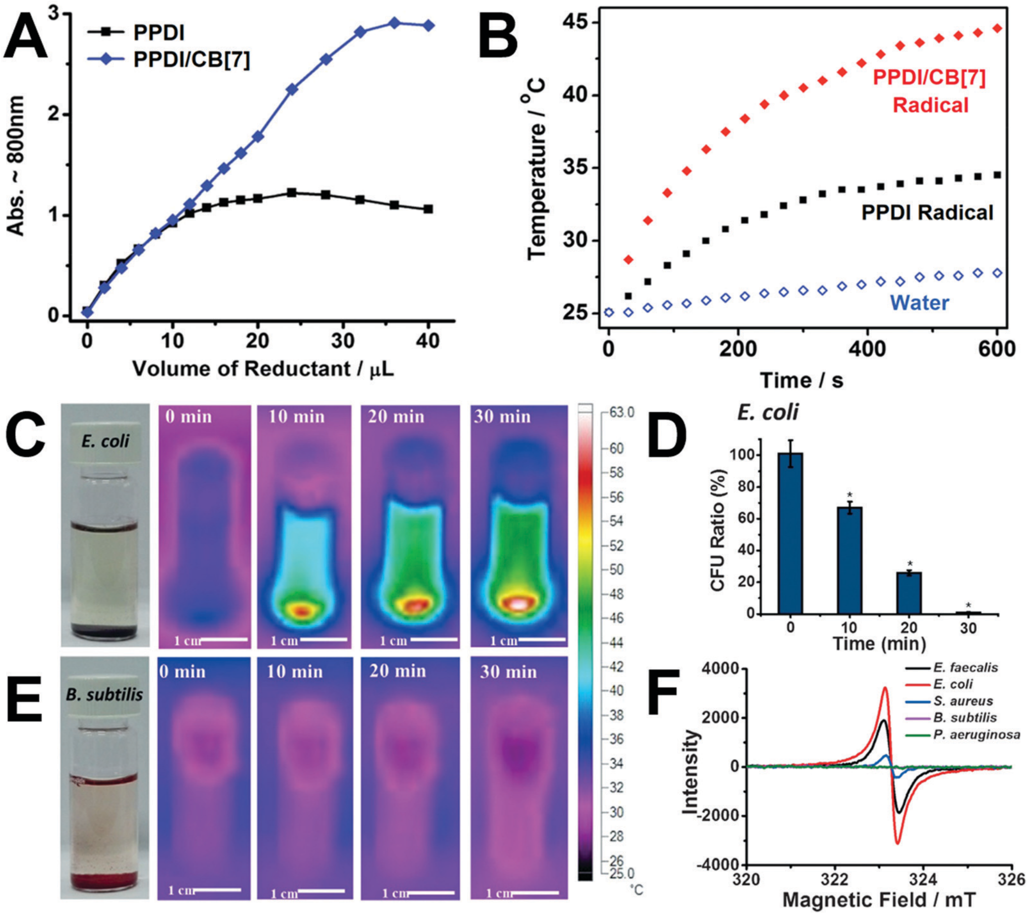

Fig. 16 (A) Radical anion concentration (determined by the intensity of the absorption peak at 800 nm) as a function of sodium dithionate reducing agent addition in PPDI and the PPDI/CB[7] supramolecular complex. (B) Photothermal conversion data of PPDI and PPDI/CB[7] radicals as a function of irradiation time with an 808 nm laser. (C) Thermal images depicting the temperature changes in aqueous PPDI/CB[7] solutions in the presence of *E. coli* under 808 nm irradiation accompanied by (D) the associated colony-forming unit (CFU) ratio. (E) Thermal images depicting temperature changes in aqueous PPDI/CB[7] solutions in the presence of *B. subtilis* under 808 nm irradiation. (F) Electron paramagnetic resonance data of PPDI/CB[7] solutions in the presence of various bacteria: *E. faecalis, E. coli, S. aureus, B. subtilis, P. aeruginosa.* Reprinted with permission from ref. 184. Copyright 2017 John Wiley & Sons Inc.

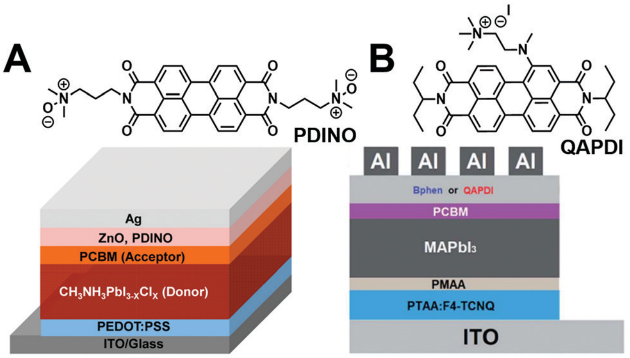

Fig. 17 (A) Chemical structure of PDINO and the relevant corresponding device stack. Reprinted with permission from ref. 206. Copyright 2015 American Chemical Society. (B) Structure of QAPDI and the relevant corresponding device stack. Reproduced from ref. 206. Copyright 2020 The Royal Society of Chemistry.

respectively, due to the favorable contact between PCBM and PDINO, whereas changes in the J_{sc} are attributed to spectral losses in the IR region. External quantum efficiency action spectra of the different devices reveal PDINO devices achieve values ∼10–20% greater than ZnO or the control in the ∼575–775 nm region. Moreover, different sweep delay times do not induce hysteresis in PDINO devices, and differences in ETL layer thickness (5–24 nm) do not significantly hinder device performance, a phenomenon commonly observed in materials >10 nm thick. The devices are also remarkably stable, retaining 90% efficiency over 300 h in air.[205] N-PDI ETLs also demonstrate excellent performance in perovskite solar cells, achieving 17.66% and 14.32% PCE in rigid and flexible cells respectively.[51]

Wang *et al.* recently reported the novel QAPDI which features a bay-substituted tertiary amine and quaternary ammonium salt in a hybrid perovskite solar cell, as shown in Fig. 17B. The absorption spectrum of QAPDI shows a broad absorption band from 500–700 nm both in solution and in thin films consistent with N-PDIs substituted at the bay position and possesses electron mobility values very close to that of PCBM in electron-only devices (1.05×10^{-3} and

1.21×10^{-3} cm^2 V^{-1} s^{-1}, respectively). The authors compare the performance of QAPDI and the commonly used 4,7-diphenyl-1,10-phenanthroline (Bphen) as ETLs in methylammonium lead iodide (MAPbI$_3$) perovskite solar cell devices (Fig. 17B). Devices with Bphen exhibit a maximum PCE of 18.6%, while QAPDI devices reach a maximum power conversion efficiency of 20.55%, which is one of the highest PCE values for PDI-inclusive devices to date. Additionally, QAPDI films exhibit a lower hysteresis index than control devices, suggesting that these layers are also able to suppress hysteresis in hybrid perovskite solar cell devices. The improved device parameters are attributable to high mobility values, improved electron injectability, reduced recombination, and improved interfacial contact in QAPDI films.[206]

4.3 Thermoelectricity

In aggregate, roughly 55–65% of the energy produced in the US is lost as waste heat, with 80% being released as heated gases from 100–300 °C.[207–209] The development of thermoelectric modules efficient at lower temperatures has received considerable attention as a means of recapturing some of this wasted heat and turning it into useful energy. The development of flexible and inexpensive organic semiconductors to meet this end is an area of rapidly growing research.[210–212] Small molecules, in particular, are attractive as they possess intrinsically low thermal conductivities, are monodisperse, and are amenable to solution processing.[213–218] There are readily discernable advantages of self-doped over extrinsically doped n-type thermoelectric systems. Thermoelectric systems are sensitive to the width of the density of states near the Fermi energy.[39] Following charge transfer, these states distort in ways that are very difficult to predict.[219] The incorporation of self-dopants axiomatically narrows the density of state width due to film matrix homogeneity. Additionally, the thermoelectric figure of merit is maximized for a specific carrier concentration within a material that possesses a given material quality factor.[220,221] Sequential doping, even at modest concentrations, can alter the morphology of thin films and change the material quality factor, thus rendering carrier concentration tuning problematic in these systems. Self-doped systems, on the other hand, have a single quality factor. Because the spin density can be thermally and photoactivated, self-doping offers a promising method of optimizing the figure of merit in a manner that has yet to be explored in depth. Russ *et al.* examined the thermoelectric properties of PDIs self-doped with quaternary trimethylammonium hydroxides with varying –(CH$_2$)$_n$ tether length between the core and the dopant. Changing the tether length from n = 2 to 4 and 6 has little effect on the Seebeck coefficient (~ -200 μV K^{-1}) but dramatically increases the electrical conductivity of thin films by over two orders of magnitude from $\sim$0.001 to $\sim$0.4 S cm^{-1}. The power factor is more commonly reported in organic thermoelectric materials and is directly proportional to the thermoelectric figure of merit. The n = 6 N-PDI has a power factor of 1.4 μW mK^{-2}, which is one of the highest power factors reported in n-type small molecule organic thermoelectric materials.[81]

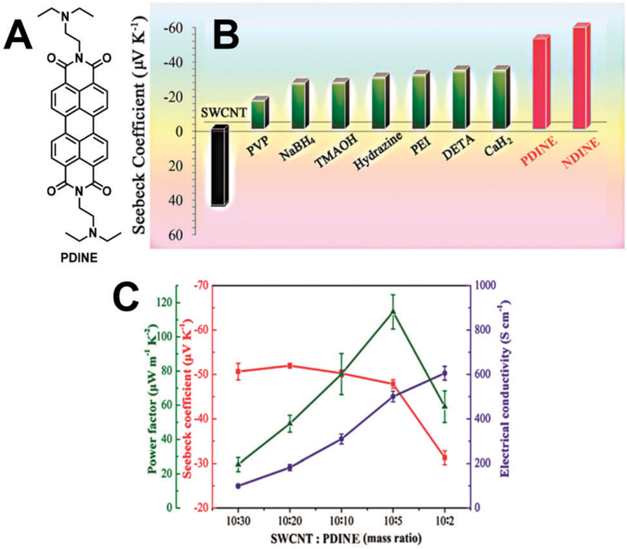

Fig. 18 (A) P/N Seebeck coefficient switching of SWCNT following modification with several n-type dopants, most notably with (B) PDINE and NDINE. (C) Electrical conductivity (blue), Seebeck coefficient (red), and power factor (green) of SWCNT:PDINE composites at various mass ratios. (Note: polyvinylpyrrolidone [PVP], trimethylammonium hydroxide [TMAOH], poly(ether imide) [PEI], diethylenetriamine [DETA]). Reprinted with permission from ref. 53. Copyright 2017 American Chemical Society.

N-PDIs can also be incorporated into composite materials. Work by Wu *et al.* has shown promising results in this regard. A composite thermoelectric material composed of high-conductivity single-walled carbon nanotubes (SCWNT) and PDINE (Fig. 18A) combines the excellent properties of these two materials. The Seebeck coefficient of pristine SCWNT films (p-type) and SCWNT composite materials (n-type) with various electron dopants are shown in Fig. 18B (including a self-doped naphthalene diimide NDINE). Compared to other reducing agents, PDINE and NDINE composites have considerably larger Seebeck coefficients. The films exhibit excellent air stability for n-type semiconductors, with 83.5% conductivity remaining after 100 h of air exposure. The conductivity, Seebeck coefficient, and resulting power factor are plotted as a function of SCWNT/PDINE mass ratio in Fig. 18C. The power factor of the composite is maximized at a 10 : 5 mass ratio to 112 ± 8 μW mK^{-2} under a 50 °C temperature gradient, which is one of the highest power factors for n-type organic and organic/inorganic composite materials.[53]

4.4 Energy storage

In recent decades there has been unprecedented growth in battery-operated devices, from cellular phones and laptops to the internet of things, wearable devices for personal and medical use, and radio-frequency identification technology. Redox-active organic molecules are very attractive in battery applications because they are often capable of multi-electron transfer and could be used to create high energy density systems. Additionally, their low carbon footprint and solution processability make them likely candidates. N-type materials have shown great promise for their redox activity, and recent emphasis has been placed on increasing their intrinsic electronic conductivity to improve power density and increase mass loading to improve energy density for long-term performance improvements.[222] Additionally, many state-of-the-art organic materials are plagued by low specific capacity or are unstable to multiple cycling events.[223] An organic compound's theoretical capacity is determined by its electron affinity, while cyclability depends on the chemical reversibility of this process. It has been demonstrated that strong n-type doping of organic compounds can improve Coulombic efficiency and specific capacity.[224,225] The intrinsic n-type doping of N-PDIs, coupled with their good electron conductivity and mobility make them attractive in battery applications.

Supur *et al.* combined an N-PDI with a two-carbon tether and ammonium iodide named TAIPDI with reduced graphene oxide (RGO) to form TAIPDI/RGO composites. TAIPDI is able to then self-assemble onto the surface of the graphene, as previously reported.[226] Thermogravimetric analysis of the individual components and the TAIPDI/RGO composite show that TAIPDI decomposes at a higher temperature in the composites, demonstrating electrostatic interaction between the respective species. Scanning electron micrographs of TAIPDI/RGO show even dispersion of TAIPDI on the surface of graphene, which could potentially be increased by self-assembly tailoring. Cathode films incorporated into lithium-ion batteries were constructed with 80 wt% composite, 15 wt% carbon, and 5 wt% polyvinylidene fluoride binder. The devices exhibit a specific capacity of 81.5 mA h g^{-1} at a current density of 25 mA g^{-1} and retain 73% of the initial reversible capacity after 500 cycles. The Coulombic efficiency of the half-cell remains at ~99% for the duration of the 500 cycles at 25 mA g^{-1}, implying long life cycles for the composites.[227] Graphene/N-PDI composites have also been used as sodium battery cathode materials, and the interested reader is directed here.[54]

The lack of an efficient and scalable large-scale energy storage solution that can stabilize the intermittency of renewable electricity sources is rapidly becoming a pressing issue. Redox flow batteries (RFBs) have garnered attention in recent years as they are seen as one of the most attractive targets for stationary energy storage with a high capacity for industrial scaling.[228,229] However, widespread adoption is restricted due to high cost and use of low abundance of hazardous materials. Organic RFBs are thus attractive but have lagged behind due to

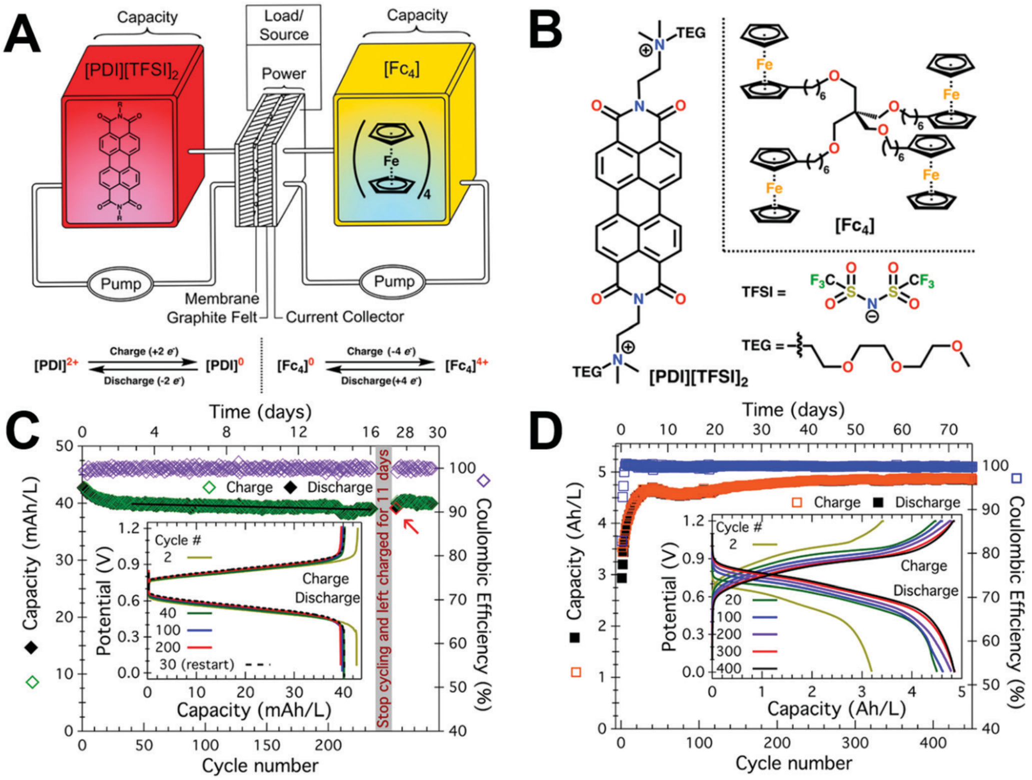

Fig. 19 (A) Schematic diagram of the redox flow battery and the corresponding redox reactions of [PDI][TFSI]$_2$ and [Fc$_4$], whose structures are given in (B). (C) Output performance of a low concentration cell comprised of 1.17 mM [Fc$_4$] and 1.8 mM [PDI][TFSI]$_2$. The Coulombic efficiency (purple diamonds) has an average of 99.955%. Repeated charge (green diamonds)/discharge (black diamonds) cycling at 1C over >230 cycles in a stirred H-cell configuration. The first discharge (red diamond) and selected charge/discharge profiles for the cell (inset) are also displayed. (D) Output performance of a high concentration cell comprised of 100 mM [Fc$_4$] and 200 mM [PDI][TFSI]$_2$. The Coulombic efficiency (blue squares) has an average of 99.868% above cycle 5. Repeated charge (orange square)/discharge (black square) capacities over >450 cycles corresponding to >74 days of operation, along with selected charge/discharge profiles for the cell (inset), is shown. Li[TFSI] was used as a supporting electrolyte in both cells C and D, and the voltage was limited from 0 to 1.2 V. Reprinted with permission from ref. 231. Copyright 2017 American Chemical Society.

the instability of the charged electrolytes.[230] Recent work by Milton *et al.* yielded fully organic nonaqueous flow batteries comprised of a [PDI][TFSI]$_2$ anolyte coupled to a tetraferrocene [Fc$_4$] catholyte separated by a dialysis membrane (Fig. 19A and B). The RFBs were tested at both low and high concentrations. The low concentration stirred H-cell composed of 1.17 mM [Fc$_4$] and 1.8 mM [PDI][TFSI]$_2$ can sustain >230 cycles at 1C while maintaining an average Coulombic efficiency of 99.955% (Fig. 19C). The cell exhibits excellent stability, with the charge and discharge capacity settling after 40 cycles and retaining it for over 200 with very little fade. Additionally, the cell can be left in its charged state for 11 days without any capacity loss due to the stability of the radicals that form during operation. The high concentration cell tested in Fig. 19D is comprised of 0.1 M [Fc$_4$] and 0.2 M [PDI][TFSI]$_2$, equivalent to 0.4 mol electron/liter, which rivals that of benchmark organic media RFBs. The high concentration cell exhibits steady performance over >450 cycles with an average Coulombic efficiency of 99.868% and 68% energy efficiency.[231] It should be noted that PDIs generally suffer from a low energy density due to their undesirable redox potential (-0.7 V *vs.* Ag/Ag$^+$). Future work in this area to widen the potential window and PDI solubility will likely lead to the realization of practical RFBs incorporating N-PDIs.

4.5 Photocatalysis

Photosynthesis is the primary source of atmospheric oxygen, and its importance in evolutionary history cannot be overstated. Artificial photosynthesis with molecular catalysts aims to produce carbon-neutral fuel feedstocks through a variety of reactions, such as water splitting or hydrogen reduction.[232,233] Compounds that form long-lived photoinduced charge transfer states are commonly used in artificial photosynthesis.[234] Photoelectrochemical methods of converting solar energy into electrical energy have attracted considerable attention in recent years due to their cost-efficiency over photovoltaic/electrolyzer systems, but require materials able to withstand harsh photo-corrosive environments.[235] The excellent photostability, large molar extinction coefficient, strong π-stacking, and amphiphilic structure of PDIs make them excellent candidates for photoelectrochemical catalytic systems. For solar water splitting, the most demanding portion of the reaction is the 4-electron reduction of water, and powerfully oxidizing holes are required to drive the reaction forward.[236] While the use of oxidative metal oxide photoanodes was known, Ronconi *et al.* developed a strategy of sensitizing WO$_3$ and SnO$_2$ by soaking the oxides in acetonitrile solutions containing PDI$^+$PF$_6$$^-$ (Fig. 20A) for improved photoanodic current. The coordination of PDI$^+$PF$_6$$^-$ to porous WO$_3$, TiO$_2$, and SnO$_2$ results in blue-shifted H-aggregate absorption features of PDI$^+$PF$_6$$^-$ on the metal oxide surfaces and strongly positive holes as verified by cyclic voltammetry ($E_{\mathrm{ox}} \sim 1.7$ V *vs.* SCE). In the presence of an acetonitrile/0.1 M LiI sacrificial reductant, the photoanodic current increases upon photoirradiation, consistent with electron injection from PDI$^+$PF$_6$$^-$ to the metal oxide and hole transfer from the reductant to PDI$^+$PF$_6$$^-$ as shown in Fig. 20B. The largest photocurrent of 0.5 mA cm^{-2} is that of PDI$^+$PF$_6$$^-$/WO$_3$ under a 0.35 V bias *vs.* SCE. The injection rates are estimated with time-correlated single-photon counting to be $k_{\mathrm{inj}}(\mathrm{WO_3}) = 0.4 \times 10^9\ \mathrm{s^{-1}}$, $k_{\mathrm{inj}}(\mathrm{SnO_2}) = 0.1 \times 10^9\ \mathrm{s^{-1}}$, and $k_{\mathrm{inj}}(\mathrm{TiO_2}) = 0.05 \times 10^9\ \mathrm{s^{-1}}$. The performance of the composite photoanodes is thus attributed to electron injectability. PDI$^+$PF$_6$$^-$/WO$_3$ photoanodes were functionalized with IrO$_2$ nanoparticles under various processing conditions as an example water oxidation catalyst (Fig. 20C). Under 1.5 G illumination in 0.1 M NaClO$_4$ and pH = 3 (no sacrificial reductant), the co-deposited electrodes exhibit photocurrent close to 70 μA cm^{-2} at 0.5 V *vs.* SCE. The presence of IrO$_2$ increases the photocurrent density $\sim$6-fold in comparison with PDI$^+$PF$_6$$^-$/WO$_3$ electrodes alone due to the efficient hole transfer from photogenerated PDI$^+$PF$_6$$^-$ to IrO$_2$.[58] Sensitized PDI$^+$PF$_6$$^-$/SnO$_2$ photoanodes have also been studied for HBr splitting as an alternative H$_2$ solar fuel production method, and the interested reader is directed here.[237,238] Tertiary amine nanofibers have also been used as TiO$_2$ photoanode sensitizers for the photoelectrocatalytic generation of hydrogen gas. In aqueous 0.2 M HCl electrolyte and triethylamine as a sacrificial hole trap, a

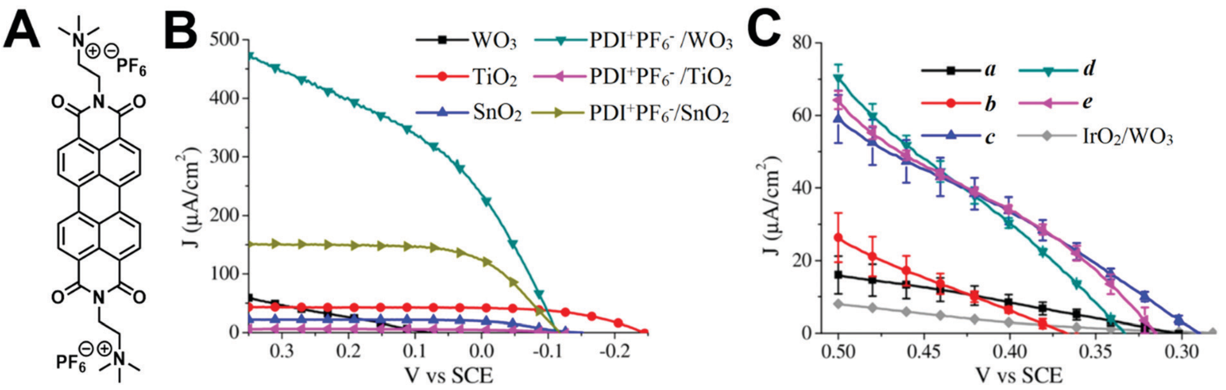

Fig. 20 (A) Chemical structure of PDI$^+$PF$_6$$^-$. (B) *J*–*V* curves of electrodes with and without the application of the PDI$^+$PF$_6$$^-$ sensitizer in the presence of acetonitrile/0.1 M LiI. The current densities shown are obtained by subtracting their respective dark currents. (C) *J*–*V* curves of different batches of PDI$^+$PF$_6$$^-$/WO$_3$ photoelectrodes with (b–e) and without (a) and IrO$_2$ modifier. Reprinted with permission from ref. 58. Copyright 2015 American Chemical Society.

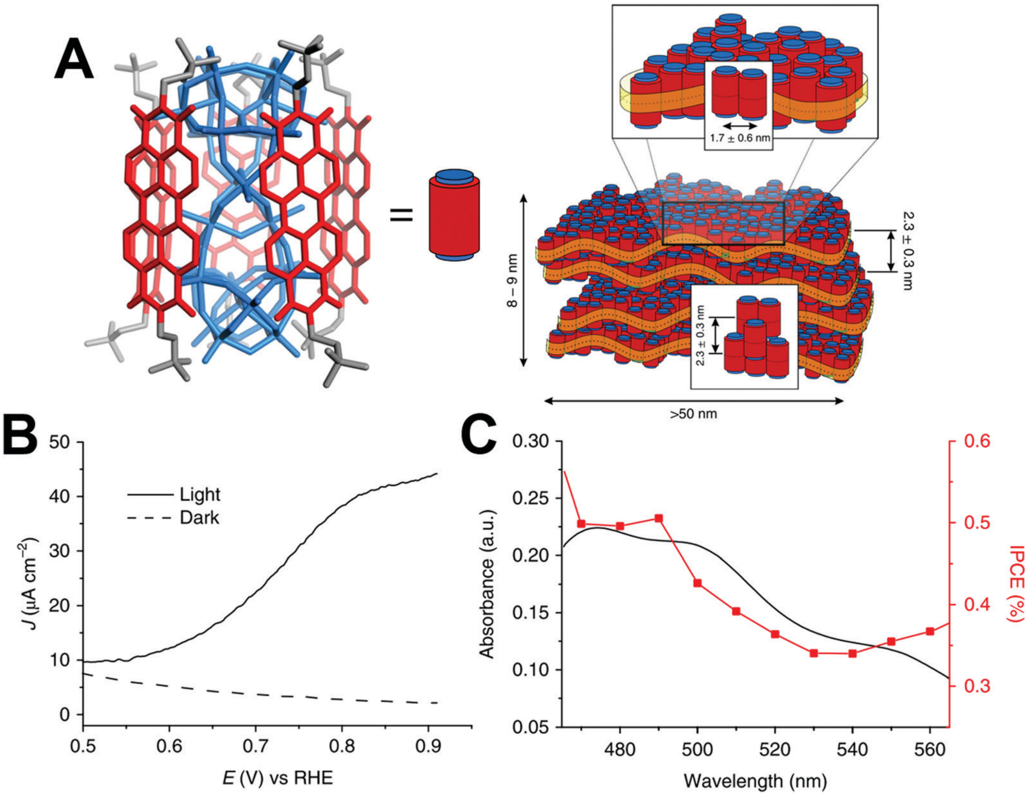

Fig. 21 (A) Representation of the $[PDI]_5Ru_4POM$ coordination complex as a cylindrical amphiphile with the Ru_4POM building block shown in blue, the aromatic PDI in red, and the alkylammonium tails in grey. Additionally, the hierarchical ordering of these complexes into nanolamellae and their mean separation distances are shown. (B) Photocurrent density (solid) compared to dark current density (dashed) of a $NanoWO_3|\{[PDI]_5Ru_4POM\}_n$ as a function of applied potential under simulated solar irradiation in aqueous HClO4 pH 3, 0.1 M NaClO4. (C) Action spectrum of a $NanoWO_3|\{[PDI]_5Ru_4POM\}_n$ photoanode showing the absorption spectrum (black) overlaid with the internal power conversion efficiency (red) as a function of irradiation wavelength. Reprinted with permission from ref. 49. Copyright 2018 Springer Nature.

maximum photocurrent of $\sim$40 μA cm^{-2} at 0.6 V *vs.* Ag/AgCl is obtained to generate 4–8 μmol h^{-1} g^{-1}, which is also an excellent benchmark in comparison to similar systems.[239] Similar work has been done on phosphonate substituted PDIs by Kirner *et al.*, offering an interesting strategy of altering N-PDIs by exchanging nitrogen with heavier pnictogens.[240]

Beyond sensitizing photoanodes, N-PDIs can also directly sensitize the catalyst. Dicationic *N*,*N*′-bis(2-(trimethylammonium)ethylene)perylene-3,4,9,10-tetracarboxylic acid diimide can be directly coordinated to the polyoxometalate $[Ru_4(\mu\text{-}O)_4(\mu\text{-}OH)_2(H_2O)_4(\gamma\text{-}SiW_{10}O_{36})_2]^{10-}$ (Ru_4POM) deca-anion as a biomimetic quantasome photosystem II water oxidation catalyst. Ru_4POM has a low overpotential of 300–350 mV, a wide operational pH range of 1–7, and ultrafast photoinduced electron transfer, making it an attractive target for PDI functionalization.[241] PDI readily coordinates to the Ru_4POM catalyst in water, with 5 PDIs units to each Ru_4POM to form $[PDI]_5Ru_4POM$ as core-shell cylindrical amphiphiles (Fig. 21A). Small and wide-angle X-ray scattering reveals that these cylinders pack closely together with a mosaicity of 10–15° in a paracrystalline phase which then stack into 2D lamellar superstructures. $[PDI]_5Ru_4POM$ can then be templated onto nanostructured WO_3 photoanodes to create a regenerative photoelectrochemical cell. Photoelectrochemical cell measurements of $NanoWO_3|\{[PDI]_5Ru_4POM\}_n$ were done in aqueous 1 mM $HClO_4$/0.1 M $NaClO_4$ at pH = 3 in the 0.51–0.91 V *vs.* RHE potential window at 20 mV s^{-1} under 1.5 G illumination ($\lambda > 450$ nm). The onset potential of the photoelectrochemical cell under illumination is near the saturation plateau of $>$40 μA cm^{-2} at $<$0.6 V and 0.91 V revealing fast hole scavenging and catalysis, as shown in Fig. 21B. The incident photon-to-current efficiency action spectrum aligns with the absorption spectrum of $\{[PDI]_5Ru_4POM\}_n$ with the peak 0.5% efficiency in the same range as the absorption maximum (Fig. 21C). The absorbed photon-to-current efficiency of the photoelectrochemical cell is found to be $\sim$1.3% in the 470–540 nm range.[49] This considerably outperformed other state-of-the-art Ru_4POM sensitized photoanodes.[58,242,243] N-PDIs thus act as efficient sensitizers of both photoanodes and catalysts in photoelectrochemical cells.

5. Conclusion and outlook

We have reviewed the intrinsic properties of PDIs, and how these are altered by the incorporation of electron-rich moieties. PDIs are one of the most extensively utilized organic scaffolds in semiconductor research due to their excellent photostability, tunability, and photophysical properties. Many structural modifications to the PDI scaffold do not significantly alter the physicochemical properties of the chromophore. However, the incorporation of tertiary amines or quaternary ammonium substituents at the bay or imide positions creates self-n-doped N-PDIs capable of radical anion and dianion formation. The self-n-doping character of N-PDIs, coupled with their amphiphilic nature separates this class from other structural derivatives, and they have demonstrated remarkable promise across a wide breadth of fields, including biochemistry, energy harvesting, and energy storage. We have discussed how doping efficiency in N-PDIs depends on the dopant architecture, attachment distance, and attachment mode to the PDI core.

In recent years, an increasingly diverse range of self-n-doped materials have appeared in the literature, many exhibiting benchmark performances in numerous applications. However, little attention has been paid to establishing self-dopant design principles. Dopant structure-function relationships are in their infancy. It is not clearly understood why certain architectures undergo structural degradation nor how degradation affects device performance. Many new approaches may be taken to modify the dopant architecture, such as aromatization, structural rigidity, or substitution of heavier pnictogens. These modifications can also be paired with modifications to the host, such as carbonyl thionation. As with other n-type materials, one of the major challenges to be addressed is improving air stability, which could be enhanced by modifying the PDI core scaffold. A thorough understanding of these features would likely enable further performance enhancements beyond those that have already been realized. Additionally, a deeper understanding of the relationship between dopant architecture and its influence on self-assembly is lacking. The literature regarding self-n-doping materials is often fragmented by intended application, leading some researchers to neglect amine/ammonium doping or even wrongly attribute doping to other species present in their systems. It is our hope that this work will inform and encourage others to study the many unique and often surprising behaviors of self-n-doped materials.

Conflicts of interest

There are no conflicts to declare.

Acknowledgements

The authors would like to acknowledge financial support from the NSF under awards # DMR 1824263 and # CBET 2016191. LWB would also like to acknowledge the Sloan Foundation through an Alfred P. Sloan Research Fellowship in Chemistry and the Dreyfus Foundation through a Camille Dreyfus Teacher-Scholar Award. The authors also gratefully acknowledge Steven Powell for his artistic contributions to the manuscript.

References

1 I. Salzmann, G. Heimel, M. Oehzelt, S. Winkler and N. Koch, *Acc. Chem. Res.*, 2016, **49**, 370–378.

2 I. Salzmann, G. Heimel, S. Duhm, M. Oehzelt, P. Pingel, B. M. George, A. Schnegg, K. Lips, R. P. Blum, A. Vollmer and N. Koch, *Phys. Rev. Lett.*, 2012, **108**, 1–5.

3 V. A. Kolesov, C. Fuentes-Hernandez, W.-F. Chou, N. Aizawa, F. A. Larrain, M. Wang, A. Perrotta, S. Choi, S. Graham, G. C. Bazan, T.-Q. Nguyen, S. R. Marder and B. Kippelen, *Nat. Mater.*, 2016, **1**, 1–8.

4 I. Salzmann and G. Heimel, *J. Electron Spectrosc. Relat. Phenom.*, 2015, **204**, 208–222.

5 R. A. Schlitz, F. G. Brunetti, A. M. Glaudell, P. L. Miller, M. A. Brady, C. J. Takacs, C. J. Hawker and M. L. Chabinyc, *Adv. Mater.*, 2014, **26**, 2825–2830.

6 J. Liu, L. Qiu, G. Portale, M. Koopmans, G. ten Brink, J. C. Hummelen and L. J. A. Koster, *Adv. Mater.*, 2017, **29**, 1–8.

7 L. Qiu, J. Liu, R. Alessandri, X. Qiu, M. Koopmans, R. W. A. Havenith, S. J. Marrink, R. C. Chiechi, L. J. Anton Koster and J. C. Hummelen, *J. Mater. Chem. A*, 2017, **5**, 21234–21241.

8 M. L. Tietze, J. Benduhn, P. Pahner, B. Nell, M. Schwarze, H. Kleemann, M. Krammer, K. Zojer, K. Vandewal and K. Leo, *Nat. Commun.*, 2018, **9**, 1–9.

9 Y. Ikenoue, J. Chiang, A. O. Patil, F. Wudl and A. J. Heeger, *J. Am. Chem. Soc.*, 1988, **110**, 2983–2985.

10 C. K. Mai, R. A. Schlitz, G. M. Su, D. Spitzer, X. Wang, S. L. Fronk, D. G. Cahill, M. L. Chabinyc and G. C. Bazan, *J. Am. Chem. Soc.*, 2014, **136**, 13478–13481.

11 V. V. Kondratiev and R. Holze, *Chem. Pap.*, 2021, **75**, 4981–5007.

12 D. R. G. Brimage and R. S. Davidson, *J. Chem. Soc. D: Chem. Commun.*, 1971, 1385–1386.

13 T. Okada, M. Migita, N. Mataga, Y. Sakata and S. Misumi1, *J. Am. Chem. Soc.*, 1981, **103**, 4715–4720.

14 G. Schnurpfeil, J. Stark and D. Whörle, *Dyes Pigm.*, 1995, **27**, 339–350.

15 B. Riichiro Ide, Y. Sakata, S. Misumi, T. Okada, N. Mataga, A. Chandross and H. T. Thomas, *Intramolecular Exciplex Formation in Some Compounds Containing Condensed Aromatic Hydrocarbon and NN-Dimethylaniline Moieties*, 1972, vol. 9.

16 L. J. Andrews, *Chem. Rev.*, 1954, **54**, 713–776.

17 J. S. Miller and J. C. Calabrese, *J. Chem. Soc., Chem. Commun.*, 1988, 63–64.

18 E. Amerling, Y. Zhai, B. W. Larson, Y. Yao, B. Fluegel, Z. Owczarczyk, H. Lu, L. Whittaker-Brooks, V. Blum and J. L. Blackburn, *J. Mater. Chem. A*, 2021, **9**, 14977–14990.

19 J. J. Liu, Y. F. Guan, C. Jiao, M. J. Lin, C. C. Huang and W. X. Dai, *Dalton Trans.*, 2015, **44**, 5957–5960.

20 A. H. Proppe, M. H. Tremblay, Y. Zhang, Z. Yang, R. Quintero-Bermudez, S. O. Kelley, S. Barlow, S. R. Marder and E. H. Sargent, *J. Phys. Chem. C*, 2020, **124**, 24379–24390.

21 M. H. Tremblay, A. M. Zeidell, S. Rigin, C. Tyznik, J. Bacsa, J. Bacsa, Y. Zhang, K. Al Kurdi, O. D. Jurchescu,

T. V. Timofeeva, S. Barlow and S. R. Marder, *Inorg. Chem.*, 2020, **59**, 8070–8080.

22 J. Jia, B. Fan, M. Xiao, T. Jia, Y. Jin, Y. Li, F. Huang and Y. Cao, *Macromol.*, 2018, **51**, 2195–2202.

23 S. Wang, Z. Li, X. Xu, M. Zhang, G. Zhang, Y. Li and Q. Peng, *J. Mater. Chem. A*, 2018, **6**, 22503–22507.

24 B. H. Lee, I. H. Jung, H. Y. Woo, H. K. Shim, G. Kim and K. Lee, *Adv. Funct. Mater.*, 2014, **24**, 1100–1108.

25 C. Gao, Y. Liu, Y. Gao, Y. Zhou, X. Zhou, X. Yin, C. Pan, C. Yang, H. Wang, G. Chen and L. Wang, *J. Mater. Chem. A*, 2018, **6**, 20161–20169.

26 S. K. Keshri, K. Mandal, Y. Kumar, D. Yadav and P. Mukhopadhyay, *Chem. – Eur. J.*, 2021, **27**, 6954–6962.

27 H. Tang, Z. Liu, Y. Tang, Z. Du, Y. Liang, Z. Hu, K. Zhang, F. Huang and Y. Cao, *Giant*, 2021, **6**, 100053.

28 C. Z. Li, C. C. Chueh, H. L. Yip, F. Ding, X. Li and A. K. Y. Jen, *Adv. Mater.*, 2013, **25**, 2457–2461.

29 C. Zhao, C. G. Tang, Z. L. Seah, Q. M. Koh, L. L. Chua, R. Q. Png and P. K. H. Ho, *Nat. Commun.*, 2021, **12**, 1–9.

30 C. G. Tang, M. C. Y. Ang, K. K. Choo, V. Keerthi, J. K. Tan, M. N. Syafiqah, T. Kugler, J. H. Burroughes, R. Q. Png, L. L. Chua and P. K. H. Ho, *Nature*, 2016, **539**, 536–540.

31 K. M. O'Malley, C. Z. Li, H. L. Yip and A. K. Y. Jen, *Adv. Energy Mater.*, 2012, **2**, 82–86.

32 X. Sun, W. Chen, L. Liang, W. Hu, H. Wang, Z. Pang, Y. Ye, X. Hu, Q. Wang, X. Kong, Y. Jin and M. Lei, *Chem. Mater.*, 2016, **28**, 8726–8731.

33 C. Bradley and M. C. Lonergan, *J. Mater. Chem. A*, 2016, **4**, 8777–8783.

34 W. Chen, W. Jiao, D. Li, X. Sun, X. Guo, M. Lei, Q. Wang and Y. Li, *Chem. Mater.*, 2016, **28**, 1227–1235.

35 W. Jiao, D. Ma, M. Lv, W. Chen, H. Wang, J. Zhu, M. Lei and X. Chen, *J. Mater. Chem. A*, 2014, **2**, 14720–14728.

36 C. G. Tang, M. N. Syafiqah, Q. M. Koh, C. Zhao, J. Zaini, Q. J. Seah, M. J. Cass, M. J. Humphries, I. Grizzi, J. H. Burroughes, R. Q. Png, L. L. Chua and P. K. H. Ho, *Nature*, 2019, **573**, 519–525.

37 E. B. Faulkner and R. J. Schwartz, *High Performance Pigments*, Wiley, 2nd edn, 2009.

38 A. Mishra and P. Bäuerle, *Angew. Chem., Int. Ed.*, 2012, **51**, 2020–2067.

39 B. Russ, A. Glaudell, J. J. Urban, M. L. Chabinyc and R. A. Segalman, *Nat. Rev. Mater.*, 2016, **1**, 1–14.

40 X. Zhan, A. Facchetti, S. Barlow, T. J. Marks, M. A. Ratner, M. R. Wasielewski and S. R. Marder, *Adv. Mater.*, 2011, **23**, 268–284.

41 F. Würthner, *Pure Appl. Chem.*, 2006, **78**, 2341–2349.

42 T. Weil, T. Vosch, J. Hofkens, K. Peneva and K. Müllen, *Angew. Chem., Int. Ed.*, 2010, **49**, 9068–9093.

43 Q. Wang, Z. Li, D. D. Tao, Q. Zhang, P. Zhang, D. P. Guo and Y. B. Jiang, *Chem. Commun.*, 2016, **52**, 12929–12939.

44 F. Würthner, C. R. Saha-Möller, B. Fimmel, S. Ogi, P. Leowanawat and D. Schmidt, *Chem. Rev.*, 2016, **116**, 962–1052.

45 A. Weißenstein, C. R. Saha-Möller and F. Würthner, *Chem. – Eur. J.*, 2018, **24**, 8009–8016.

46 W. Ji, X. Zhang, J. Zhao, Y. Gao, W. Song and Y. Ozaki, *Analyst*, 2018, **143**, 1899–1905.

47 T. Takada, A. Ashida, M. Nakamura and K. Yamana, *Bioorg. Med. Chem.*, 2013, **21**, 6011–6014.

48 M. Franceschin, E. Pascucci, A. Alvino, D. D. Ambrosio, A. Bianco, M. Savino, L. Sapienza, P. A. Moro and D. Chimica, *Bioorg. Med. Chem. Lett.*, 2007, **17**, 2515–2522.

49 M. Bonchio, Z. Syrgiannis, M. Burian, N. Marino, E. Pizzolato, K. Dirian, F. Rigodanza, G. A. Volpato, G. la Ganga, N. Demitri, S. Berardi, H. Amenitsch, D. M. Guldi, S. Caramori, C. A. Bignozzi, A. Sartorel and M. Prato, *Nat. Chem.*, 2019, **11**, 146–153.

50 G. Echue, G. C. Lloyd-Jones and C. F. J. Faul, *Chem. – Eur. J.*, 2015, **21**, 5118–5128.

51 H. Zhang, L. Xue, J. Han, Y. Q. Fu, Y. Shen, Z. Zhang, Y. Li and M. Wang, *J. Mater. Chem. A*, 2016, **4**, 8724–8733.

52 Z. Hu, R. Xu, S. Dong, K. Lin, J. Liu, F. Huang and Y. Cao, *Mater. Horiz.*, 2017, **4**, 88–97.

53 G. Wu, Z. Zhang, Y. Li, C. Gao, X. Wang and G. Chen, *ACS Nano*, 2017, **11**, 5746–5752.

54 T. Huang, D. Lu, L. Ma, X. Xi, R. Liu and D. Wu, *Chem. Eng. J.*, 2018, **349**, 66–71.

55 T. H. Reilly, A. W. Hains, H. Y. Chen and B. A. Gregg, *Adv. Energy Mater.*, 2012, **2**, 455–460.

56 R. F. Fink, J. Seibt, V. Engel, M. Renz, M. Kaupp, S. Lochbrunner, H. M. Zhao, J. Pfister, F. Würthner and B. Engels, *J. Am. Chem. Soc.*, 2008, **130**, 12858–12859.

57 W. E. Ford and P. V. Kamat, *J. Phys. Chem.*, 1987, **91**, 6373–6380.

58 F. Ronconi, Z. Syrgiannis, A. Bonasera, M. Prato, R. Argazzi, S. Caramori, V. Cristino and C. A. Bignozzi, *J. Am. Chem. Soc.*, 2015, **137**, 4630–4633.

59 F. Würthner, *Chem. Commun.*, 2004, 1564–1579.

60 J. Mizuguchi and K. Tojo, *J. Phys. Chem. B*, 2002, **106**, 767–772.

61 K. E. Brown, W. A. Salamant, L. E. Shoer, R. M. Young and M. R. Wasielewski, *J. Phys. Chem. Lett.*, 2014, **5**, 2588–2593.

62 H. Langhals, *Heterocycles*, 1995, **40**, 477–500.

63 M. Supur and S. Fukuzumi, *Phys. Chem. Chem. Phys.*, 2013, **15**, 2539–2546.

64 A. J. Tilley, R. D. Pensack, T. S. Lee, B. Djukic, G. D. Scholes and D. S. Seferos, *J. Phys. Chem. C*, 2014, **118**, 9996–10004.

65 T. J. Ryan, R. M. Young, J. J. Henkelis, N. Hafezi, N. A. Vermeulen, A. Hennig, E. J. Dale, Y. Wu, M. D. Krzyaniak, A. Fox, W. M. Nau, M. R. Wasielewski, J. F. Stoddart and O. A. Scherman, *J. Am. Chem. Soc.*, 2015, **137**, 15299–15307.

66 V. Nguyen, S. Qi, S. Kim, N. Kwon, G. Kim, Y. Yim, S. Park and J. Yoon, *J. Am. Chem. Soc.*, 2019, **141**, 16243–16248.

67 A. J. Tilley, C. Guo, M. B. Miltenburg, T. B. Schon, H. Yan, Y. Li and D. S. Seferos, *Adv. Funct. Mater.*, 2015, **25**, 3321–3329.

68 N. T. la Porte, J. F. Martinez, S. Hedström, B. Rudshteyn, B. T. Phelan, C. M. Mauck, R. M. Young, V. S. Batista and M. R. Wasielewski, *Chem. Sci.*, 2017, **8**, 3821–3831.

69 D. Gosztola, M. P. Niemczyk, W. Svec, A. S. Lukas and M. R. Wasielewski, *J. Phys. Chem. A*, 2000, **104**, 6545–6551.

70 A. Segalina, X. Assfeld, A. Monari and M. Pastore, *J. Phys. Chem. C*, 2019, **123**, 6427–6437.
71 M. Kasha, *Radiat. Res.*, 1963, **20**, 55–70.
72 M. Kasha, *Rev. Mod. Phys.*, 1959, **31**, 162–169.
73 P. M. Kazmaier and R. Hoffmann, *J. Am. Chem. Soc.*, 1994, **116**, 9684–9691.
74 N. J. Hestand and F. C. Spano, *Chem. Rev.*, 2018, **118**, 7069–7163.
75 N. J. Hestand and F. C. Spano, *Acc. Chem. Res.*, 2017, **50**, 341–350.
76 M. Burian, F. Rigodanza, H. Amenitsch, L. Almásy, I. Khalakhan, Z. Syrgiannis and M. Prato, *Chem. Phys. Lett.*, 2017, **683**, 454–458.
77 K. Bag, R. Halder, B. Jana and S. Malik, *J. Phys. Chem. C*, 2019, **123**, 6241–6249.
78 P. Lasitha and E. Prasad, *Chem. – Eur. J.*, 2016, **22**, 10558–10564.
79 M. Hoffmann, K. Schmidt, T. Fritz, T. Hasche, V. M. Agranovich and K. Leo, *Chem. Phys.*, 2000, **258**, 73–96.
80 J. Li, H. Zhou, Y. Zhang, S. A. Shahzad, M. Yang, Z. Hu and C. Yu, *Anal. Chim. Acta*, 2018, **1016**, 40–48.
81 B. Russ, M. J. Robb, F. G. Brunetti, P. L. Miller, E. E. Perry, S. N. Patel, V. Ho, W. B. Chang, J. J. Urban, M. L. Chabinyc, C. J. Hawker and R. A. Segalman, *Adv. Mater.*, 2014, **26**, 3473–3477.
82 B. A. Gregg, S. G. Chen and R. A. Cormier, *Chem. Mater.*, 2004, **16**, 4586–4599.
83 S. G. Chen, H. M. Branz, S. S. Eaton, P. C. Taylor, R. A. Cormier and B. A. Gregg, *J. Phys. Chem. B*, 2004, **108**, 17329–17336.
84 B. A. Gregg, S. G. Chen and H. M. Branz, *Appl. Phys. Lett.*, 2004, **84**, 1707–1709.
85 B. A. Gregg and R. A. Cormier, *J. Am. Chem. Soc.*, 2001, **123**, 7959–7960.
86 M. Supur, Y. M. Sung, D. Kim and S. Fukuzumi, *J. Phys. Chem. C*, 2013, **117**, 12438–12445.
87 A. El-Refaey, S. Y. Shaban, M. El-Kemary and M. E. El-Khouly, *Spectrochim. Acta, Part A*, 2017, **186**, 132–139.
88 A. Weißenstein, C. R. Saha-Möller and F. Würthner, *Chem. – Eur. J.*, 2018, **24**, 8009–8016.
89 Y. Che, X. Yang, G. Liu, C. Yu, H. Ji, J. Zuo, J. Zhao and L. Zang, *J. Am. Chem. Soc.*, 2010, **132**, 5743–5750.
90 P. S. Hariharan, J. Pitchaimani, V. Madhu and S. P. Anthony, *J. Fluroresc.*, 2016, **26**, 395–401.
91 H. Yongwei, Q. Baogang, W. Zhixiang, L. Guangtong and S. Lianfeng, *J. Phys. Chem. C*, 2009, **113**, 3929–3933.
92 E. Tenori, A. Colusso, Z. Syrgiannis, A. Bonasera, S. Osella, A. Ostric, R. Lazzaroni, M. Meneghetti and M. Prato, *ACS Appl. Mater. Interfaces*, 2015, **7**, 28042–28048.
93 Y. Huang, X. Liu, Q. Wang, J. Fu, L. Zhao, Z. Liu and D. Jin, *J. Mater. Chem. C*, 2017, **5**, 7644–7651.
94 B. Pramanik, J. H. Mondal, N. Singha, S. Ahmed, J. Mohanty and D. Das, *ChemPhysChem*, 2017, **18**, 245–252.
95 B. Roy, T. Noguchi, D. Yoshihara, T. Yamamoto, J. Sakamoto and S. Shinkai, *Phys. Chem. Chem. Phys.*, 2016, **18**, 13239–13245.
96 L. Ma, W. Gao, X. Han, F. Qu, L. Xia and R. M. Kong, *New J. Chem.*, 2019, **43**, 3383–3389.
97 B. Wang, Q. Zhu, D. Liao and C. Yu, *J. Mater. Chem.*, 2011, **21**, 4821–4826.
98 L. Zang, R. Liu, M. W. Holman, K. T. Nguyen and D. M. Adams, *J. Am. Chem. Soc.*, 2002, **124**, 10640–10641.
99 G. J. Mohr, U. E. Spichiger, W. Jona and H. Langhals, *Anal. Chem.*, 2000, **72**, 1084–1087.
100 N. Wu, C. Wang, B. R. Bunes, Y. Zhang, P. M. Slattum, X. Yang and L. Zang, *ACS Appl. Mater. Interfaces*, 2016, **8**, 12360–12368.
101 C. Rodríguez-Abreu, C. Aubery-Torres, C. Solans, A. López-Quintela and G. J. T. Tiddy, *ACS Appl. Mater. Interfaces*, 2011, **3**, 4133–4141.
102 G. Panzarasa, A. L. Torzynski, T. Sai, K. Smith-Mannschott and E. R. Dufresne, *Soft Matter*, 2020, **16**, 591–594.
103 C. Rodríguez-Abreu, C. Aubery-Torres, C. Solans, A. López-Quintela and G. J. T. Tiddy, *ACS Appl. Mater. Interfaces*, 2011, **3**, 4133–4141.
104 T. A. Everett and D. A. Higgins, *Langmuir*, 2009, **25**, 13045–13051.
105 M. Supur and S. Fukuzumi, *J. Phys. Chem. C*, 2012, **116**, 23274–23282.
106 A. Weißenstein and F. Würthner, *Chem. Commun.*, 2015, **51**, 3415–3418.
107 Y. Guan, S. H. Yu, M. Antonietti, C. Böttcher and C. F. J. Faul, *Chem. – Eur. J.*, 2005, **11**, 1305–1311.
108 C. Rodriguez-Abreu, N. Vilanova, C. Solans, M. Ujihara, T. Imae, A. López-Quintela and S. Motojima, *Nanoscale Res. Lett.*, 2011, **6**, 1–7.
109 C. R. Weitzel, T. A. Everett and D. A. Higgins, *Langmuir*, 2009, **25**, 1188–1195.
110 X. Tang, Y. Yang, Y. Kang, H. Wu, J. F. Xu and Z. Wang, *Langmuir*, 2020, **36**, 5954–5959.
111 D. Görl, X. Zhang and F. Würthner, *Angew. Chem., Int. Ed.*, 2012, **51**, 6328–6348.
112 O. P. Boiko, B. Ya, O. Yu, Y. L. Slominskiy, S. A. Tsybulia, Y. A. Nastishin and V. G. Nazarenko, *Synth. Met.*, 2019, **257**, 116147.
113 Y. Zakrevskyy, C. F. J. Faul, Y. Guan and J. Stumpe, *Adv. Funct. Mater.*, 2004, **14**, 835–841.
114 I. K. Iverson, S. M. Casey, W. Seo, S. W. Tam-Chang and B. A. Pindzola, *Langmuir*, 2002, **18**, 3510–3516.
115 A. Laiho, B. M. Smarsly, C. F. J. Faul and O. Ikkala, *Adv. Funct. Mater.*, 2008, **18**, 1890–1897.
116 S. W. Tam-Chang, I. K. Iverson and J. Helbley, *Langmuir*, 2004, **20**, 342–347.
117 S. W. Tam-Chang, J. Helbley and I. K. Iverson, *Langmuir*, 2008, **24**, 2133–2139.
118 S. Shin, E. Chang, S. Lee, J. Ku and K. Jeong, *Thin Solid Films*, 2011, **520**, 486–490.
119 Y. Guan, Y. Zakrevskyy, J. Stumpe and C. F. J. Faul, *Chem. Commun.*, 2003, 894–895.
120 P. V. Soroka, A. Y. Vakhnin, Y. A. Skryshevskiy, O. P. Boiko, M. I. Anisimov, Y. L. Slominskiy, V. G. Nazarenko, J. Genoe and A. Kadashchuk, *EPJ Appl. Phys.*, 2014, **68**, 1–9.

121 H. J. Kim, W. Jung, H. S. Jeong and H. Jung, *J. Mater. Chem. C*, 2017, **5**, 12241–12248.
122 I. Ghosh, T. Ghosh, J. I. Bardagi and B. König, *Science*, 2014, **346**, 725–728.
123 Y. Matsunaga, K. Goto, K. Kubono, K. Sako and T. Shinmyozu, *Chem. – Eur. J.*, 2014, **20**, 7309–7316.
124 J. M. Giaimo, A. v Gusev and M. R. Wasielewski, *J. Am. Chem. Soc.*, 2002, **124**, 8530–8531.
125 T. D. Anthopoulos, G. C. Anyfantis, G. C. Papavassiliou and D. M. de Leeuw, *Appl. Phys. Lett.*, 2007, **90**, 122105.
126 F. S. Goodson, D. K. Panda, S. Ray, A. Mitra, S. Guha and S. Saha, *Org. Biomol. Chem.*, 2013, **11**, 4797–4803.
127 B. Russ, M. J. Robb, B. C. Popere, E. E. Perry, C.-K. Mai, S. L. Fronk, S. N. Patel, T. E. Mates, G. C. Bazan, J. J. Urban, M. L. Chabinyc, C. J. Hawker and R. A. Segalman, *Chem. Sci.*, 2016, **7**, 1914–1919.
128 Z. Wang, N. Zheng, W. Zhang, H. Yan, Z. Xie, Y. Ma, F. Huang and Y. Cao, *Adv. Energy Mater.*, 2017, **7**, 1–7.
129 A. S. Lukas, Y. Zhao, S. E. Miller and M. R. Wasielewski, *J. Phys. Chem. B*, 2002, **106**, 1299–1306.
130 H. Liu, G. Yin, Q. Li, G. Liu, S. Pu and H. Zhang, *Dyes Pigm.*, 2019, **165**, 319–326.
131 B. Rybtchinski, L. E. Sinks and M. R. Wasielewski, *J. Phys. Chem. A*, 2004, 7497–7505.
132 Y. Zhao and M. R. Wasielewski, *Tetrahedron Lett.*, 1999, **40**, 7047–7050.
133 H. Langhals and P. Blanke, *Dyes Pigm.*, 2003, **59**, 109–116.
134 F. Bureš, *RSC Adv.*, 2014, **4**, 58826–58851.
135 M. J. Ahrens, M. J. Tauber and M. R. Wasielewski, *J. Org. Chem.*, 2006, **71**, 2107–2114.
136 H. Wu, H. Wang, L. Xue, Y. Shi and X. Li, *J. Phys. Chem. B*, 2010, 14420–14425.
137 P. van Haver, N. Helsen, S. Depaemelaere, M. van der Auweraer and F. C. de Schryver, *J. Am. Chem. Soc.*, 1991, **113**, 6849–6857.
138 A. M. Swinnen, M. van der Auweraer, F. C. de Schryver, K. Nakatani, T. Okada and N. Malaga, *J. Am. Chem. Soc.*, 1987, **109**, 321–330.
139 E. Hussain, H. Zhou, N. Yang, S. Anjum and C. Yu, *Dyes Pigm.*, 2017, **147**, 211–224.
140 M. E. Ozser, S. A. Sarkodie, O. Mohiuddin and G. Ozesme, *J. Lumin.*, 2017, **192**, 414–423.
141 A. D. Scaccabarozzi, A. Basu, F. Aniés, J. Liu, O. Zapata-Arteaga, R. Warren, Y. Firdaus, M. I. Nugraha, Y. Lin, M. Campoy-Quiles, N. Koch, C. Müller, L. Tsetseris, M. Heeney and T. D. Anthopoulos, *Chem. Rev.*, 2022, **122**, 4420–4492.
142 D. Powell, Z. Rhodes, X. Zhang, E. J. Miller, M. Jonely, K. R. Hansen, C. I. Nwachukwu, A. G. Roberts, H. Wang, R. Noriega, S. D. Minteer and L. Whittaker-Brooks, *ACS Mater. Au*, 2022, DOI: **10.1021/acsmaterialsau.2c00019**.
143 Y. Song, W. Zhang, S. He, L. Shang, R. Ma, L. Jia and H. Wang, *ACS Appl. Mater. Interfaces*, 2019, **11**, 33676–33683.
144 L. Zhan, L. J. Liang, S. J. Zhen, C. M. Li and C. Z. Huang, *Analyst*, 2013, **138**, 825–830.
145 E. Maltas, S. Malkondu, P. Uyar and M. Ozmen, *Mater. Sci. Eng., C*, 2015, **48**, 86–93.
146 D. D'Ambrosio, P. Reichenbach, E. Micheli, A. Alvino, M. Franceschin, M. Savino and J. Lingner, *Biochim.*, 2012, **94**, 854–863.
147 A. Alvino, M. Franceschin, C. Cefaro, S. Borioni and C. Biomolecolare, *Tetrahedron*, 2007, **63**, 7858–7865.
148 Y. Liu, X. Gao, F. Lu, M. Hu, L. Shi and L. Zheng, *Soft Matter*, 2017, **13**, 3072–3075.
149 H. Zhao, S. Hussain, X. Liu, S. Li, F. Lv and L. Liu, *Chem. – Eur. J.*, 2019, **100049**, 9834–9839.
150 G. Echue, I. Hamley, G. C. L. Jones and C. F. J. Faul, *Langmuir*, 2016, **32**, 9023–9032.
151 J. Gershberg, M. Radić Stojković, M. Škugor, S. Tomić, T. H. Rehm, S. Rehm, C. R. Saha-Möller, I. Piantanida and F. Würthner, *Chem. – Eur. J.*, 2015, **21**, 7886–7895.
152 D. Han, J. Han, S. Huo, Z. Qu, T. Jiao, M. Liu and P. Duan, *Chem. Commun.*, 2018, **54**, 5630–5633.
153 Y. Huang, Y. Yan, B. M. Smarsly, Z. Wei and C. F. J. Faul, *J. Mater. Chem.*, 2009, **19**, 2356–2362.
154 Z. Lv, J. Liu, W. Bai, S. Yang and A. Chen, *Biosens. Bioelectron.*, 2015, **64**, 530–534.
155 B. Wang and C. Yu, *Angew. Chem., Int. Ed.*, 2010, **49**, 1485–1488.
156 B. Wang, H. Jiao, W. Li and D. Liao, *Chem. Commun.*, 2011, **47**, 10269–10271.
157 D. Liao, W. Li, J. Chen, H. Jiao and H. Zhou, *Anal. Chim. Acta*, 2013, **797**, 89–94.
158 R. Hu, T. Liu, X. Zhang, S. Huan, C. Wu, T. Fu and W. Tan, *Anal. Chem.*, 2014, **86**, 5009–5016.
159 S. Bettini, Z. Syrgiannis, R. Pagano, D. Luka, L. Salvatore, M. Prato, G. Giancane and L. Valli, *ACS Appl. Mater. Interfaces*, 2019, **11**, 17079–17089.
160 X. Wu, X. Chen, B. Song, Y. Huang, Z. Li and Z. Chen, *Chem. – Eur. J.*, 2014, **20**, 11793–11799.
161 X. Dai, Q. Li, A. Aldalbahi, L. Wang, C. Fan and X. Liu, *Nano Lett.*, 2020, **20**, 5604–5615.
162 L. Liang, Y. Fu, D. Wang, Y. Wei, N. Kobayashi and T. Minari, *Appl. Sci.*, 2018, **8**, 3–11.
163 H.-W. Fink and C. Schoenenberger, *Nature*, 1999, **398**, 407–410.
164 R. Carmieli, T. A. Zeidan, R. F. Kelley, Q. Mi, F. D. Lewis and M. R. Wasielewski, *J. Phys. Chem. A*, 2009, **113**, 4691–4700.
165 M. Hariharan, Y. Zheng, H. Long, T. A. Zeidan, G. C. Schatz, J. Vura-Weis, M. R. Wasielewski, X. Zuo, D. M. Tiede and F. D. Lewis, *J. Am. Chem. Soc.*, 2009, **131**, 5920–5929.
166 P. P. Neelakandan, T. A. Zeidan, M. McCullagh, G. C. Schatz, J. Vura-Weis, C. H. Kim, M. R. Wasielewski and F. D. Lewis, *Chem. Sci.*, 2014, **5**, 973–981.
167 T. A. Zeidan, R. Carmieli, R. F. Kelley, T. M. Wilson, F. D. Lewis and M. R. Wasielewski, *J. Am. Chem. Soc.*, 2008, **130**, 13945–13955.
168 T. Takada, Y. Otsuka, M. Nakamura and K. Yamana, *Chem. – Eur. J.*, 2012, **18**, 9300–9304.

169 T. Takada, M. Ido, A. Ashida, M. Nakamura and M. Fujitsuka, *Chem. – Eur. J.*, 2015, **21**, 6846–6851.

170 T. Takada, A. Ashida, M. Nakamura, M. Fujitsuka, T. Majima and K. Yamana, *J. Am. Chem. Soc.*, 2014, **136**, 6814–6817.

171 M. Franceschin, C. Bombelli, S. Borioni, G. Bozzuto, S. Eleuteri, G. Mancini, A. Molinari and A. Bianco, *New J. Chem.*, 2013, **37**, 2166–2173.

172 O. Y. Fedoroff, M. Salazar, H. Han, V. V. Chemeris, S. M. Kerwin and L. H. Hurley, *Biochemistry*, 1998, **37**, 12367–12374.

173 L. Rossetti, M. Franceschin, A. Bianco, G. Ortaggi and M. Savino, *Bioorg. Med. Chem. Lett.*, 2002, **12**, 2527–2533.

174 N. Kaewtunjai, R. Summart, A. Wongnoppavich, B. Lojanapiwat, T. R. Lee and W. Tuntiwechapikul, *Biol. Pharm. Bull.*, 2019, **42**, 906–914.

175 S. M. Kerwin, G. Chen, J. T. Kern and P. Wang Thomas, *Bioorg. Med. Chem. Lett.*, 2002, **12**, 447–450.

176 E. Micheli, A. Altieri, L. Cianni, C. Cingolani, S. Iachettini, A. Bianco, C. Leonetti, S. Cacchione, A. Biroccio, M. Franceschin and A. Rizzo, *Biochim.*, 2016, **125**, 223–231.

177 Z. Xu, W. Cheng, K. Guo, J. Yu, J. Shen, J. Tang, W. Yang and M. Yin, *ACS Appl. Mater. Interfaces*, 2015, **7**, 9784–9791.

178 Z. Xu, K. Guo, J. Yu, H. Sun, J. Tang, J. Shen, K. Müllen, W. Yang and M. Yin, *Small*, 2014, **10**, 4087–4092.

179 Y. Jiao, K. Liu, G. Wang, Y. Wang and X. Zhang, *Chem. Sci.*, 2015, **6**, 3975–3980.

180 B. Lü, Y. Chen, P. Li, B. Wang, K. Müllen and M. Yin, *Nat. Commun.*, 2019, **10**, 1–8.

181 P. Sun, X. Wang, G. Wang, W. Deng, Q. Shen, R. Jiang, W. Wang, Q. Fan and W. Huang, *J. Mater. Chem. B*, 2018, **6**, 3395–3403.

182 H. Li, L. Yue, L. Li, G. Liu, J. Zhang, X. Luo and F. Wu, *Colloids Surf., B*, 2021, **205**, 111841.

183 Q. Gong, J. Xing, Y. Huang, A. Wu, J. Yu and Q. Zhang, *ACS Appl. Bio Mater.*, 2020, **3**, 1607–1615.

184 Y. Yang, P. He, Y. Wang, H. Bai, S. Wang, J. Xu and X. Zhang, *Angew. Chem., Int. Ed.*, 2017, **56**, 16239–16242.

185 D. Barrio, I. Ghosh, F. Biedermann, A. I. Lazar, Y. Lan, R. J. Coulston, W. M. Nau and O. A. Scherman, *J. Am. Chem. Soc.*, 2014, **136**, 9053–9060.

186 D. Feldman and R. Margolis, Q4 2019/Q1 2020 Solar Industry Update, 2019.

187 F. Sani, S. Shafie, H. N. Lim and A. O. Musa, *Materials*, 2018, **11**, 1–17.

188 R. Xue, J. Zhang, Y. Li and Y. Li, *Small*, 2018, **14**, 1801793.

189 Q. Kang, L. Ye, B. Xu, C. An, S. J. Stuard, S. Zhang, H. Yao, H. Ade and J. Hou, *Joule*, 2019, **3**, 227–239.

190 C. Z. Li, C. C. Chueh, H. L. Yip, K. M. O'Malley, W. C. Chen and A. K. Y. Jen, *J. Mater. Chem.*, 2012, **22**, 8574–8578.

191 T. Jia, C. Sun, R. Xu, Z. Chen, Q. Yin, Y. Jin, H. L. Yip, F. Huang and Y. Cao, *ACS Appl. Mater. Interfaces*, 2017, **9**, 36070–36081.

192 X. Jin, Y. Wang, X. Cheng, H. Zhou, L. Hu, Y. Zhou, L. Chen and Y. Chen, *J. Mater. Chem. A*, 2018, **6**, 423–433.

193 X. Yin, X. Liu, Y. Peng, W. Zeng, C. Zhong, G. Xie, L. Wang, J. Fang and C. Yang, *Adv. Funct. Mater.*, 2019, **29**, 1806124.

194 Y. Liu, M. Sheri, M. D. Cole, D. M. Yu, T. Emrick and T. P. Russell, *Angew. Chem., Int. Ed.*, 2019, **131**, 5733–5737.

195 R. Sorrentino, E. Kozma, S. Luzzati and R. Po, *Energy Environ. Sci.*, 2021, **14**, 180–223.

196 Z. Hu, R. Xu, S. Dong, K. Lin, J. Liu, F. Huang and Y. Cao, *Mater. Horiz.*, 2017, **4**, 88–97.

197 M. Supur, Y. Kawashima, K. Mase, K. Ohkubo, T. Hasobe and S. Fukuzumi, *J. Phys. Chem. C*, 2015, **119**, 13488–13495.

198 Q. Chen, B. J. Worfolk, T. C. Hauger, U. Al-Atar, K. D. Harris and J. M. Buriak, *ACS Appl. Mater. Interfaces*, 2011, **3**, 3962–3970.

199 Z. Xie, B. Xiao, Z. He, W. Zhang, X. Wu, H. Wu, F. Würthner, C. Wang, F. Xie, L. Liu, Y. Ma, W. Y. Wong and Y. Cao, *Mater. Horiz.*, 2015, **2**, 514–518.

200 Z. G. Zhang, B. Qi, Z. Jin, D. Chi, Z. Qi, Y. Li and J. Wang, *Energy Environ. Sci.*, 2014, **7**, 1966–1973.

201 B. Qiu, J. Yuan, X. Xiao, D. He, L. Qiu, Y. Zou, Z. G. Zhang and Y. Li, *ACS Appl. Mater. Interfaces*, 2015, **7**, 25237–25246.

202 C. Weng, L. Gao, Z. Zhang, Z. Liu, S. Tan and Y. Li, *J. Polym. Sci., Part B: Polym. Phys.*, 2017, **55**, 990–996.

203 C. Song, X. Liu, X. Li, Y. C. Wang, L. Wan, X. Sun, W. Zhang and J. Fang, *ACS Appl. Mater. Interfaces*, 2018, **10**, 14986–14992.

204 Y. Ye, B. Lü, W. Cheng, Z. Wu, J. Wei and M. Yin, *Chem. – Asian J.*, 2017, **12**, 1020–1024.

205 J. Min, Z. Zhang, Y. Hou, C. Omar, R. Quiroz, T. Przybilla, C. Bronnbauer, F. Guo, K. Forberich, H. Azimi, T. Ameri, E. Spiecker, Y. Li and C. J. Brabec, *Chem. Mater.*, 2015, **27**, 227–234.

206 H. Wang, J. Song, J. Qu, J. Lian, P.-C. Qian and W.-Y. R. Wong, *J. Mater. Chem. A*, 2020, **8**, 18117–18124.

207 R. Freer and A. v Powell, *J. Mater. Chem. C*, 2020, **8**, 441–463.

208 A. Zevalkink, D. M. Smiadak, J. L. Blackburn, A. J. Ferguson, M. L. Chabinyc, O. Delaire, J. Wang, K. Kovnir, J. Martin, L. T. Schelhas, T. D. Sparks, S. D. Kang, M. T. Dylla, G. J. Snyder, B. R. Ortiz and E. S. Toberer, *Appl. Phys. Rev.*, 2018, **5**, 021303.

209 R. Kroon, D. A. Mengistie, D. Kiefer, J. Hynynen, J. D. Ryan, L. Yu and C. Müller, *Chem. Soc. Rev.*, 2016, **45**, 6147–6164.

210 G. Zuo, Z. Li, E. Wang and M. Kemerink, *Adv. Electron. Mater.*, 2018, **4**, 1–6.

211 Y. Chen, Y. Zhao and Z. Liang, *Energy Environ. Sci.*, 2015, **8**, 401–422.

212 S. Lin, W. Li, Z. Chen, J. Shen, B. Ge and Y. Pei, *Nat. Commun.*, 2016, **7**, 10287.

213 L. M. Cowen, J. Atoyo, M. J. Carnie, D. Baran and B. C. Schroeder, *ECS J. Solid State Sci. Technol.*, 2017, **6**, N3080–N3088.

214 G.-H. Kim, L. Shao, K. Zhang and K. P. Pipe, *Nat. Mater.*, 2013, **12**, 719–723.

215 M. Chabinyc, *Nat. Mater.*, 2014, **13**, 119–121.

216 R. Sato, Y. Kiyota, T. Kadoya, T. Kawamoto and T. Mori, *RSC Adv.*, 2016, **6**, 41040–41044.

217 G. Kim and K. P. Pipe, *Phys. Rev. B: Condens. Matter Mater. Phys.*, 2012, **86**, 1–5.

218 D. Wang, W. Shi, J. Chen, J. Xi and Z. Shuai, *Phys. Chem. Chem. Phys.*, 2012, **14**, 16505–16520.
219 B. Lüssem, M. Riede and K. Leo, *Phys. Status Solidi A*, 2013, **210**, 9–43.
220 S. Dongmin Kang and G. Jeffrey Snyder, *Nat. Mater.*, 2016, **16**, 252–257.
221 G. J. Snyder and E. S. Toberer, *Nat. Mater.*, 2008, **7**, 105–114.
222 Y. Lu and J. Chen, *Nat. Rev. Chem.*, 2020, **4**, 127–142.
223 S. Muench, A. Wild, C. Friebe, B. Häupler, T. Janoschka and U. S. Schubert, *Chem. Rev.*, 2016, **116**, 9438–9484.
224 M. E. Bhosale and K. Krishnamoorthy, *Chem. Mater.*, 2015, **27**, 2121–2126.
225 Q. Zhao, C. Guo, Y. Lu, L. Liu, J. Liang and J. Chen, *Ind. Eng. Chem. Res.*, 2016, **55**, 5795–5804.
226 M. Supur, K. Ohkubo and S. Fukuzumi, *Chem. Commun.*, 2014, **50**, 13359–13361.
227 W. Deng, J. Yu, Y. Qian, R. Wang, Z. Ullah, S. Zhu, M. Chen, W. Li, Y. Guo, Q. Li and L. Liu, *Electrochim. Acta*, 2018, **282**, 24–29.
228 Y. Zhao, Y. Ding, Y. Li, L. Peng, H. R. Byon, J. B. Goodenough and G. Yu, *Chem. Soc. Rev.*, 2015, **44**, 7968–7996.
229 Z. Rhodes, J. R. Cabrera-Pardo, M. Li and S. D. Minteer, *Isr. J. Chem.*, 2021, **61**, 101–112.
230 Y. Ding and G. Yu, *Angew. Chem., Int. Ed.*, 2017, **129**, 8738–8740.
231 M. Milton, Q. Cheng, Y. Yang, C. Nuckolls, R. Hernández Sánchez and T. J. Sisto, *Nano Lett.*, 2017, **17**, 7859–7863.
232 B. Zhang and L. Sun, *Chem. Soc. Rev.*, 2019, **48**, 2216–2264.
233 V. Balzani, A. Credi and M. Venturi, *ChemSusChem*, 2008, **1**, 26–58.
234 P. J. Hore, K. L. Ivanov and M. R. Wasielewski, *J. Chem. Phys.*, 2020, **152**, 120401.
235 J. T. Kirner and R. G. Finke, *J. Mater. Chem. A*, 2017, **5**, 19560–19592.
236 P. Novák, K. Müller, K. S. V. Santhanam and O. Haas, *Chem. Rev.*, 1997, **97**, 207–281.
237 S. Berardi, V. Cristino, M. Canton, R. Boaretto, R. Argazzi, E. Benazzi, L. Ganzer, R. Borrego Varillas, G. Cerullo, Z. Syrgiannis, F. Rigodanza, M. Prato, C. A. Bignozzi and S. Caramori, *J. Phys. Chem. C*, 2017, **121**, 17737–17745.
238 E. Benazzi, K. Rettenmaier, T. Berger, S. Caramori, S. Berardi, R. Argazzi, M. Prato and Z. Syrgiannis, *J. Phys. Chem. C*, 2020, **124**, 1317–1329.
239 L. Yang, M. Wang, P. M. Slattum, B. R. Bunes, Y. Wang, C. Wang and L. Zang, *ACS Appl. Mater. Interfaces*, 2018, **10**, 19764–19772.
240 J. T. Kirner, J. J. Stracke, B. A. Gregg and R. G. Finke, *ACS Appl. Mater. Interface*, 2014, **6**, 13367–13377.
241 Y. Liu, S. X. Guo, A. M. Bond, J. Zhang, Y. V. Geletii and C. L. Hill, *Inorg. Chem.*, 2013, **52**, 11986–11996.
242 Y. H. Lai, M. Kato, D. Mersch and E. Reisner, *Faraday Discuss.*, 2014, **176**, 199–211.
243 J. Fielden, J. M. Sumliner, N. Han, Y. V. Geletii, X. Xiang, D. G. Musaev, T. Lian and C. L. Hill, *Chem. Sci.*, 2015, **6**, 5531–5543.